

## Ocean Turbulence. Part II: Vertical Diffusivities of Momentum, Heat, Salt, Mass, and Passive Scalars

V. M. CANUTO

*NASA Goddard Institute for Space Studies and Department of Applied Physics, Columbia University, New York, New York*

A. HOWARD, Y. CHENG, AND M. S. DUBOVIKOV

*NASA Goddard Institute for Space Studies, New York, New York*

(Manuscript received 31 July 2000, in final form 21 June 2001)

### ABSTRACT

A Reynolds stress–based model is used to derive algebraic expressions for the vertical diffusivities  $K_\alpha$  ( $\alpha = m, h, s$ ) for momentum, heat, and salt. The diffusivities are expressed as

$$K_\alpha(R_\rho, N, \text{Ri}^T, \epsilon)$$

in terms of the density ratio  $R_\rho = \alpha_s \partial S / \partial z (\alpha_T \partial T / \partial z)^{-1}$ , the Brunt–Väisälä frequency  $N^2 = -g\rho_0^{-1} \partial \rho / \partial z$ , the Richardson number  $\text{Ri}^T = N^2 / \Sigma^2$  ( $\Sigma$  is the shear), and the dissipation rate of kinetic energy  $\epsilon$ . The model is valid both in the mixed layer (ML) and below it. Here  $R_\rho$  and  $N$  are computed everywhere using the large-scale fields from an ocean general circulation model while  $\text{Ri}^T$  is contributed by resolved and unresolved shear. In the ML, the wind-generated large-scale shear dominates and can be computed within an OGCM. Below the ML, the wind is no longer felt and small-scale shear dominates. In this region, the model provides a new relation  $\text{Ri}^T = cf(R_\rho)$  with  $c \approx 1$  in lieu of Munk's suggestion  $\text{Ri}^T \approx c$ . Thus, below the ML, the  $K_\alpha$  become functions of  $R_\rho$ ,  $N$ , and  $\epsilon$ .

The dissipation  $\epsilon$  representing the physical processes responsible for the mixing, which are different in different parts of the ocean, must also be expressed in terms of the large-scale fields. In the ML, the main source of stirring is the wind but below the ML there is more than one possible source of stirring. For regions away from topography, one can compute  $\epsilon$  using a model for internal waves. On the other hand, near topography, one must employ different expressions for  $\epsilon$ . In agreement with the data, the resulting diffusivities are location dependent rather than universal values.

Using North Atlantic Tracer Release Experiment (NATRE) data, the authors test the new diffusivities with and without an OGCM. The measured diffusivities are well reproduced. Also, a set of global  $T$  and  $S$  profiles is computed using this model and the KPP model. The profiles are compared with Levitus data. In the North Atlantic, at 24°N, the meridional overturning is close to the measured values of  $17 \pm 4$  Sv and  $16 \pm 5$  Sv ( $\text{Sv} \equiv 10^6 \text{ m}^3 \text{ s}^{-1}$ ). The polar heat transport for the North Atlantic Ocean, the Indo–Pacific Ocean, and the global ocean are generally lowered by double diffusion. The freshwater budget is computed and compared with available data.

### 1. Introduction: Physical motivation

In Canuto et al. (2001b, hereafter Part I) we employed the Reynolds stress formalism to construct a model for the heat and momentum diffusivities. The goal of this paper is to extend the same formalism to include double diffusive processes, that is, the possibility that heat and salt diffusivity may differ. Although we are not the first to study this problem (Gargett and Holloway 1992; Zhang et al. 1999; Zhang and Schmitt 2000), there are two motivations for a new treatment. First, the NATRE data (North Atlantic Tracer Release Experiment: Led-

well et al. 1993, 1998) have provided the first set of measured salt, heat, and tracer diffusivities at different ocean depths. The second motivation is of methodological nature: recent advances in turbulence modeling allow a unified treatment of momentum, heat, and salt with the same formalism. Thus, the use in an OGCM of a diffusivity model that has been tested on the NATRE data may help answer the question of Ledwell et al. (1998): how are the heat and salt diffusivities  $K_h$  and  $K_s$  modulated by the density ratio  $R_\rho$  and what effect does this modulation have on the general circulation?

Using the Reynolds stress formalism, we derive algebraic expressions for the diffusivities  $K_{m,h,s}$  (momentum, heat, salt) as functions of  $N$  (Brunt–Väisälä frequency),  $R_\rho$  (density ratio),  $\text{Ri}^T$  (Richardson number), and  $\epsilon$  (dissipation rate of kinetic energy):

---

Corresponding author address: Dr. V. M. Canuto, NASA Goddard Institute for Space Studies, 2880 Broadway, New York, NY 10025.  
E-mail: acvmc@giss.nasa.gov

$$K_\alpha(R_\rho, N, Ri^T, \epsilon), \quad \alpha = m, h, s. \quad (1a)$$

Relations (1a) are valid both in the mixed layer (ML) and below it. While the functions  $R_\rho$  and  $N$  are computable everywhere using the large-scale temperature and salinity fields from an OGCM,  $Ri^T$  is contributed by both large-scale (resolved) and small-scale (unresolved) shear. In the ML (mixed layer), the strongest shear is the wind-generated large-scale shear, which is computable within an OGCM. Below the ML, where the wind effects are no longer felt, it is the small-scale shear generated by internal waves that dominates. In that regime, the present model provides a new relation  $Ri^T = cf(R_\rho)$  with  $c \approx 1$  in lieu of Munk's suggestion that  $Ri^T \approx c$ . Thus, below the ML, Eq. (1a) reduces to

$$K_\alpha(R_\rho, N, \epsilon), \quad \alpha = m, h, s. \quad (1b)$$

The dissipation  $\epsilon$ , which is not computed by an OGCM, plays a physically important role. Since mixing requires a source of energy, there is a necessity to exhibit the energy required to sustain the mixing processes. This point has been discussed by Munk and Wunsch (1998), Wunsch (2000), and Egbert and Ray (2000).

The available sources of energy are different at different depths and in different parts of the ocean and so are the resulting diffusivities. In the ML, the primary energy source is the wind shear, while below the ML there are several energy sources. Figure 3 of Ledwell et al. (2000) shows deep ocean diffusivities at various locations. For example, at the NATRE site (away from boundaries) the diffusivities are around  $\sim 0.1 \text{ cm}^2 \text{ s}^{-1}$  while values 40 times larger were measured in the Brazilian Basin (Polzin et al. 1997). Internal wave breaking processes are thought to be the primary source of mixing in the open ocean, and models exist that provide the corresponding  $\epsilon$  (e.g., the Gregg–Heneyey–Polzin model). However, the  $\epsilon$  representing tidal dissipation over topography (Bell 1975; Armi and Millard 1976; Müller and Xu 1992; Jayne and St. Laurent 2001) or geothermal heating on global ocean circulation (Adcroft et al. 2001) requires appropriate models describing those processes.

Over the years, relations (1b) were represented with different models. Gargett and Holloway (1992) used a constant  $K_s/K_h$  ratio. Large et al. (1994) used  $K_s/K_h = 1.43$  but Merryfield et al. (1999) pointed out that the correct relation is  $K_s/K_h = 1.43R_\rho^{-1}$ . Zhang et al. (1988, hereafter ZHS) used phenomenological expressions for  $K_{h,s}(R_\rho)$  (Schmitt 1981; Kunze 1987, 1990; Fedorov 1988; Kelley 1984, 1990), but St. Laurent and Schmitt (1999, Fig. 16) showed that two such models (Kunze 1987, 1990) predict an  $R_\rho$  dependence not in accord with NATRE data; the ad hoc model by Schmitt (1981) has the correct  $R_\rho$  dependence but is too diffusive. All authors find that double diffusion lowers the meridional transport.

The structure of the paper is as follows. In sections 2 to 8 we derive the expressions for the diffusivities  $K_\alpha$  and discuss the physics of the model and the role of the

dissipation timescales, the weak and strong mixing regimes, the existence of a critical  $R_\rho(\text{cr})$  above which one has strong salt fingers, and the inclusion of the internal wave field. In section 10, we compare ours with previous models and in section 11 we discuss general features of the diffusivities. In sections 12 and 13 we compare the model results with NATRE data with and without an OGCM. In section 14 we exhibit the  $T$ – $S$  profiles for the global ocean (and for different ocean basins), the meridional streamfunction, the polar heat transport, and the freshwater budgets. In sections 15 and 16 we present a discussion and future improvements of the model.

## 2. Diffusivities: General features

Global ocean models solve the dynamic equations for the large-scale velocity  $U_i$ , temperature  $T$ , and salinity  $S$  (in Cartesian coordinates,  $i$  and  $j$  take the values 1, 2, 3):

$$\frac{\partial}{\partial t} U_i + \frac{\partial}{\partial x_j} (U_i U_j + \overline{u_i'' u_j''}) = \dots \quad (2a)$$

$$\frac{\partial T}{\partial t} + \frac{\partial}{\partial x_i} (U_i T + \overline{u_i'' T''}) = \dots \quad (2b)$$

$$\frac{\partial S}{\partial t} + \frac{\partial}{\partial x_i} (U_i S + \overline{u_i'' s''}) = \dots \quad (2c)$$

Since the velocity, temperature, and salinity fields have also fluctuating components  $u_i''$ ,  $T''$ ,  $s''$ , nonlinear interactions give rise to the second order moments  $\overline{u_i'' u_j''}$  (momentum fluxes or Reynolds stresses),  $\overline{u_i'' T''}$  (heat fluxes), and  $\overline{u_i'' s''}$  (salinity fluxes). The overbar means averaging performed over the grid cell and the time step of the OGCM. A local turbulence model (in section 16 we discuss nonlocal models) provides the vertical fluxes:

$$\begin{aligned} \overline{w'' u''} &= -K_m \frac{\partial U}{\partial z}, & \overline{w'' T''} &= -K_h \frac{\partial T}{\partial z}, \\ \overline{w'' s''} &= -K_s \frac{\partial S}{\partial z}, \end{aligned} \quad (2d)$$

where  $K_\alpha$  ( $\alpha = m, h, s$ ) are the diffusivities given as a function of

$$K_\alpha = K_\alpha(R_\rho, N, Ri^T, \epsilon), \quad (2e)$$

where  $R_\rho$  is the density ratio and  $Ri^T$  is the total Richardson number:

$$R_\rho = \alpha_s \frac{\partial S}{\partial z} \left( \alpha_T \frac{\partial T}{\partial z} \right)^{-1}, \quad Ri^T = \frac{N^2}{\Sigma_T^2}. \quad (3a)$$

The  $\alpha_{TS}$  are the thermal expansion and haline contraction coefficients and

$$N^2 = -\frac{g}{\rho_0} \frac{\partial \rho}{\partial z} = g \alpha_T \frac{\partial T}{\partial z} (1 - R_\rho) = N_h^2 (1 - R_\rho). \quad (3b)$$

The total shear  $\Sigma_T = (\Sigma^2 + \Sigma'^2)^{1/2}$  is contributed by resolved large scales (that dominate in the ML) and by small unresolved scales that dominate below the ML. We have

$$\Sigma^2 = 2(\Sigma_{ij}\Sigma_{ij}), \quad \Sigma_{ij} = \frac{1}{2}\left(\frac{\partial U_i}{\partial x_j} + \frac{\partial U_j}{\partial x_i}\right). \quad (3c)$$

The diffusivities  $K_\rho$ ,  $K_c$  that enter the mass flux  $\overline{w''\rho''}$  and the concentration flux  $\overline{w''c''}$ :

$$\overline{w''\rho''} = -K_\rho \frac{\partial \rho}{\partial z}, \quad \overline{w''c''} = -K_c \frac{\partial C}{\partial z} \quad (3d)$$

are given by

$$K_\rho = (K_h - K_s R_\rho)(1 - R_\rho)^{-1} \quad (3e)$$

$$K_c = (K_s + K_h R_\rho)(1 + R_\rho)^{-1}. \quad (3f)$$

Equation (3e) follows from using  $\rho''/\rho = -\alpha_T T'' + \alpha_s s''$  in the first of (3d) and using both (2d) and (3b). Equation (3f) requires some discussion. The competing effects of the  $T$ - $S$  fields on the density  $\rho$  are reflected in the minus sign in the numerator of (3e). Here  $T$ - $S$  are active scalars since they couple to  $\rho$ , which couples to the velocity, and thus ultimately  $T$ - $S$  affect turbulence. On the other hand, a passive scalar does not affect either the density or the velocity field. For example, the SF<sub>6</sub> used at the NATRE site did not affect materially the density or the velocity field by which it was passively transported. Equation (3f) assumes that a concentration field behaves like “spiciness,” which, by definition, is density neutral.

As shown below, the Reynolds-stress-based model provides the following expressions:

$$K_\alpha = 2E^2 \epsilon^{-1} S_\alpha, \quad (4a)$$

where  $E$  is turbulent kinetic energy,  $\epsilon$  its rate of dissipation, and the dimensionless functions  $S_\alpha$  are called “structure functions” (Part I; Burchard and Bolding 2001; Burchard and Deleersnijder 2001). In studies of mixing below the ML, an alternative representation is the one due to Osborn and Cox (1972) and Osborn (1980):

$$K_\alpha = \Gamma_\alpha \epsilon N^{-2}, \quad \Gamma_\alpha \equiv \frac{1}{2}(\tau N)^2 S_\alpha, \quad (4b)$$

where  $\tau = 2E/\epsilon$  is the dynamical timescale and  $\Gamma_\alpha$  are mixing efficiencies. This representation is particularly convenient for it highlights  $\epsilon$ , which is different in different parts of the ocean. For either representation, a model is needed to provide the functions  $E$ ,  $\epsilon$ ,  $S_\alpha$ , and  $\Gamma_\alpha$ . Finally, the mixing model to be discussed below is valid for the following cases: SF (salt fingers:  $\partial S/\partial z > 0$ ,  $\partial T/\partial z > 0$ ,  $R_\rho > 0$ ,  $\text{Ri}^T > 0$ ,  $0 < R_\rho < 1$ ); DC (diffusive convection:  $\partial S/\partial z < 0$ ,  $\partial T/\partial z < 0$ ,  $R_\rho > 0$ ,  $\text{Ri}^T > 0$ ,  $1 < R_\rho$ ); DS (doubly stable:  $\partial S/\partial z < 0$ ,  $\partial T/\partial z > 0$ ,  $R_\rho < 0$ ,  $\text{Ri}^T > 0$ ); DU (doubly unstable:  $\partial S/\partial z > 0$ ,  $\partial T/\partial z < 0$ ,  $R_\rho < 0$ ,  $\text{Ri}^T < 0$ ). We recall that due to the definitions of  $\text{Ri}^T$  and  $N^2$  in Eqs. (3a,b),  $\text{Ri}^T > 0$

corresponds to dynamical stability while  $\text{Ri}^T < 0$  corresponds to dynamical instability.

### 3. The Reynolds stress model

Historically, the Reynolds stress model (RSM) has been widely used to treat turbulence problems since the early 1940s [for a series of review articles, see Gatski et al. (1993)]. In addition to engineering studies, RSM have been widely applied to atmospheric and ocean studies, primarily in the ML (Part I). In this paper, we consider mixing due to three gradients  $\partial U/\partial z$ ,  $\partial T/\partial z$ , and  $\partial S/\partial z$ . In Part I, we treated the case of velocity and temperature while Zeman and Lumley (1982, 1983) treated the case of temperature and salinity. Even with three gradients, the final expressions of the diffusivities are still algebraic. The overall procedure can be summarized as follows. Consider the Navier–Stokes equations for the velocity field and the equations for  $T$ ,  $S$ . The fields are written as the sum of a resolved (large scale) plus an unresolved (small scale) fluctuating part. Substituting and averaging leads to the equations for the resolved fields, Eqs. (2a)–(2c). To obtain the dynamic equations for the fluctuating  $u'_i$ ,  $T''$ ,  $s''$  one subtracts Eqs. (2a)–(2c) from the original equations for the full fields. Multiplying the equation for  $T''$  ( $s''$ ) by  $u'_i$  and that for  $u'_i$  by  $T''$  ( $s''$ ), and the equations for  $T''$  and  $s''$  by the same  $T''$ ,  $s''$ , averaging and summing the results, one obtains the dynamic equation for the required second-order moments  $\overline{u'_i u'_j}$ ,  $\overline{u'_i T''}$ ,  $\overline{u'_i s''}$ ,  $\overline{T''^2}$ ,  $\overline{s''^2}$ , and  $\overline{T'' s''}$ . Using the notation,  $U_{i,j} \equiv \partial U_i/\partial x_j$  and  $D/Dt \equiv \partial/\partial t + U_i \partial/\partial x_i$ , the dynamic equations are Traceless Reynolds stresses:  $b_{ij} = \overline{u'_i u'_j} - 2/3 E \delta_{ij} \equiv \tau_{ij} - (2/3)E \delta_{ij}$ :

$$\begin{aligned} \frac{D}{Dt} b_{ij} = & -\frac{8}{15} E \Sigma_{ij} - (1 - p_1) \Omega_{ij} + (1 - p_2) Z_{ij} \\ & + \frac{1}{2} g (\alpha_T L_{ij} - \alpha_s M_{ij}) - 5\tau^{-1} b_{ij}. \end{aligned} \quad (5)$$

The tensors  $L_{ij}$ ,  $M_{ij}$  represent buoyancy,  $\Omega_{ij}$  represents shear  $\Sigma_{ij}$ , and  $Z_{ij}$  represents vorticity  $2V_{ij} \equiv U_{i,j} - U_{j,i}$ . They are defined as follows:

$$\begin{aligned} L_{ij} & \equiv \lambda_i J_j^h + \lambda_j J_i^h - \frac{2}{3} \delta_{ij} \lambda_k J_k^h, \\ M_{ij} & \equiv \lambda_i J_j^s + \lambda_j J_i^s - \frac{2}{3} \delta_{ij} \lambda_k J_k^s \\ \Omega_{ij} & \equiv b_{ik} \Sigma_{jk} + b_{jk} \Sigma_{ik} - \frac{2}{3} \delta_{ij} \Sigma_{km} b_{km} \\ Z_{ij} & \equiv b_{ik} V_{jk} + b_{jk} V_{ik}, \end{aligned} \quad (6)$$

where  $\lambda_i = -(g\rho)^{-1} \partial \bar{p}/\partial x_i$ ,  $\bar{p}$  being the mean pressure. Heat flux,  $J_i^h = \overline{u'_i T''}$ :

$$\begin{aligned} \frac{D}{Dt} J_i^h &= -\tau_{ij} \frac{\partial T}{\partial x_j} - J_j^h U_{i,j} - (2\alpha_T \Psi - \alpha_s \overline{s'' T''}) \frac{\partial \bar{p}}{\partial x_i} \\ &\quad - \tau_{p\theta}^{-1} J_i^h \end{aligned} \quad (7)$$

Temperature variance,  $\Psi = \frac{1}{2} \overline{T''^2}$ :

$$\frac{D\Psi}{Dt} = -J_i^h \frac{\partial T}{\partial x_i} - 2\tau_{\theta}^{-1} \Psi \quad (8)$$

Salinity variance,  $\Phi = \frac{1}{2} \overline{s''^2}$ :

$$\begin{aligned} \frac{D}{Dt} J_i^s &= -\tau_{ij} \frac{\partial S}{\partial x_j} - J_j^s U_{i,j} - (\alpha_T \overline{T'' s''} - 2\alpha_s \Phi) \frac{\partial \bar{p}}{\partial x_i} \\ &\quad - \tau_{ps}^{-1} J_i^s \end{aligned} \quad (9)$$

Salinity flux,  $J_i^s = \overline{u_i'' s''}$ :

$$\begin{aligned} \frac{D}{Dt} J_i^s &= -\tau_{ij} \frac{\partial S}{\partial x_j} - J_j^s U_{i,j} - (\alpha_T \overline{T'' s''} - 2\alpha_s \Phi) \frac{\partial \bar{p}}{\partial x_i} \\ &\quad - \tau_{ps}^{-1} J_i^s \end{aligned} \quad (10)$$

Temperature–salinity correlation,  $\overline{T'' s''}$ :

$$\frac{D}{Dt} \overline{T'' s''} = -\left( J_i^s \frac{\partial T}{\partial x_i} + J_i^h \frac{\partial S}{\partial x_i} \right) - \tau_{s\theta}^{-1} \overline{T'' s''}. \quad (11)$$

In the absence of salt, Eqs. (5)–(11) coincide with those of Part I. In the absence of shear, they coincide with Eqs. (1) of Zeman and Lumley (1982, 1983). Before presenting the solution of Eqs. (5)–(11), it is useful to discuss their physical interpretation. We begin with Eqs. (8), (9), and (11). The time variation is governed by the combination of a source term (the first term in the right-hand side of each equation) and dissipation by molecular forces (the last term). In a thermally unstably stratified flow, the  $z$  gradient of  $T$  in (8) is negative while the  $z$  component of the heat flux is positive and the first term is positive, acting as a source. An analogous argument applies to the salt variance  $\Phi$ . In the case of the heat flux, the first term in (7), which acts as a source, is given by the interaction of the Reynolds stresses with the  $T$  gradient, the second term represents the interaction of the heat flux with shear while the third term represents the positive contribution of potential energy  $\sim \overline{T''^2}$ . Analogous interpretations apply to the other equations. The last terms in Eqs. (5)–(11) represent the overall dissipation effects. When written in units of the dynamic timescale  $\tau$ , they are denoted by

$$\pi_{1,2,3,4,5} = (\tau_{ps}, \tau_{s\theta}, \tau_s, \tau_{p\theta}, \tau_{\theta}) \tau^{-1}, \quad \tau = 2E\epsilon^{-1}. \quad (12)$$

The physical role of the  $\pi$  can be better understood after we have solved Eqs. (5)–(11).

#### 4. Solution of Eqs. (5)–(11)

We shall consider the case in which the only nonzero gradients are in the  $z$  direction,  $\partial/\partial x_i \rightarrow \delta_{i3} \partial/\partial z$ . Even so, the time-dependent Eqs. (5)–(11) are very difficult

to solve or to use in an OGCM. For that reason, we consider a quasistationary state that we approximate with  $\partial/\partial t = 0$ . Equations (5)–(11) then become a system of linear, coupled, algebraic equations, which we solved using the MAPLE V (University of Waterloo, 1981–1990; Symbolic Math Toolboxes available online at [www.mathworks.com](http://www.mathworks.com)). When  $\overline{w'' u''}$ ,  $\overline{w'' T''}$ , and  $\overline{w'' s''}$  are cast in the form (2d) and each of the  $K_\alpha$  is written as in (4a), the structure functions  $S_\alpha$  turn out to be momentum:

$$DS_m = \frac{8}{75} (12 + a_1 n^2 + a_2 n c + a_3 c^2 + a_4 n + a_5 c), \quad (13a)$$

heat:

$$\begin{aligned} DS_h &= \frac{4}{15} \pi_4 (1 + b_1 c + b_2 n) \\ &\quad \times (60 + b_3 y + b_4 c + b_5 n), \end{aligned} \quad (13b)$$

salt:

$$\begin{aligned} DS_s &= \frac{4}{15} \pi_1 (1 + b_6 c + b_7 n) \\ &\quad \times (60 + b_3 y + b_4 c + b_5 n). \end{aligned} \quad (13c)$$

The dimensionless denominator  $D$  is given by

$$\begin{aligned} D &= 24 + d_1 y n^2 + d_2 y n c + d_3 y c^2 + d_4 n^3 + d_5 n^2 c \\ &\quad + d_6 n c^2 + d_7 c^3 + d_8 y n + d_9 y c + d_{10} n^2 \\ &\quad + d_{11} n c + d_{12} c^2 + d_{13} y + d_{14} n + d_{15} c. \end{aligned} \quad (14)$$

The dimensionless functions representing stratification, salt gradient, and shear are

$$\begin{aligned} x &\equiv (\tau N)^2 (1 - R_\rho)^{-1}, \quad n = -\pi_2 \pi_3 x, \\ c &= \pi_3^2 R_\rho x, \\ y &= \frac{4}{25} x (1 - R_\rho) (\text{Ri}^T)^{-1}. \end{aligned} \quad (15)$$

The variables  $a_k$ ,  $b_k$  and  $d_k$  depend on the  $\pi$  and are given in appendices A and B.

##### a. Eddy turnover time, $\tau$

The eddy turnover time  $\tau$  entering Eqs.(15) is obtained by solving the equation for the turbulent kinetic energy  $E = \frac{1}{2} \tau_{ii}$ :

$$\frac{DE}{Dt} = P_s + P_b - \epsilon, \quad (16a)$$

where the shear and buoyancy production terms are defined as

$$\begin{aligned} P_s &= -\tau_{ij} U_{i,j}, \\ P_b &= -g \bar{\rho}^{-1} \overline{\rho'' w''} = g \alpha_T J^h - g \alpha_s J^s, \end{aligned} \quad (16b)$$

where we have used the relation  $\rho''/\rho = -\alpha_T T'' + \alpha_S S''$ . In the stationary limit, Eq. (16a) becomes production equals dissipation. Using (2d), (3a,b), and (4a), we obtain

$$2(\tau N)^{-2} \text{Ri}^T = S_m - \text{Ri}^T (1 - R_\rho)^{-1} (S_h - S_s R_\rho). \quad (16c)$$

Using the  $S_{m,h,s}$ , Eq. (16c) yields  $(\tau N)^2$ ,  $x$ ,  $n$ ,  $c$ ,  $y$ ,  $S_\alpha$ , and  $\Gamma_\alpha$  as functions of  $\text{Ri}^T$  and  $R_\rho$ .

### b. Heat to salt diffusivity ratio $K_h/K_s$

The ratio of heat to salt diffusivities has a particularly simple form. Using Eq. (3) of appendix A and Eqs. (13b,c), a short algebra gives

$$\frac{K_h}{K_s} = \frac{\pi_4}{\pi_1} \frac{1 - \pi_1 \pi_3 x R_\rho + \pi_1 \pi_2 x (1 + R_\rho)}{1 + \pi_4 \pi_5 x - \pi_2 \pi_4 x (1 + R_\rho)}. \quad (17a)$$

Since  $x \sim (\tau N)^2$ , a large  $x$  means that  $\tau > N^{-1}$ : the shortest timescale is due to the strong stratification, which makes turbulence weak. On the other hand, a small  $x$  means weak stratification and stronger turbulence. Thus, we have the asymptotic regimes weak turbulence:

$$\frac{K_h}{K_s} = \frac{(\pi_2 - \pi_3) R_\rho + \pi_2}{\pi_5 - \pi_2 - \pi_2 R_\rho} \quad (17b)$$

strong turbulence:

$$\frac{K_h}{K_s} = \frac{\pi_4}{\pi_1} = \frac{\tau_{p\theta}}{\tau_{ps}}. \quad (17c)$$

The first conclusion from (17b,c) is that the timescales  $\pi$  that contribute to the weak and strong cases are different. Purely dissipative timescales  $\tau_s$ ,  $\tau_\theta$  ( $\pi_{3,5}$ ) are expected to affect only the weak case when molecular forces are maximal and Eq. (17b) confirms the expectation. On the other hand, in the strong limit, we have only  $\tau_{p\theta}$  and  $\tau_{ps}$ , which are contributed by both molecular and pressure correlations (subscript p). The latter come about as follows. In deriving the dynamic equations for the heat and salt fluxes  $w''T''$  and  $w''S''$ , one employs the Navier–Stokes equations for  $w''$ , which entails the pressure gradient  $\partial p''/\partial z$ . Using Poisson's equation, pressure terms can be written in terms of the velocity field so as to assure that the latter is nondivergent,  $\partial u_i''/\partial x_i = 0$ . Thus, pressure correlations, when viewed as part of the nonlinear interactions, are an important component of the strong limit, as confirmed by Eq. (17c).

## 5. Critical $R_\rho$

In the ocean, salt fingers coexist with shear, which in the deep ocean and away from boundaries is due to internal wave breaking. It is therefore important to define the regimes where shear and salt fingers dominate. As for the latter, Schmitt and Evans (1978) have shown

that only “modes with  $R_\rho \geq R_\rho(\text{cr}) = 1/2$  become strongly established” and Zhang et al. (1998) state that a “reasonable value based on observations” is  $R_\rho(\text{cr}) = 0.64$  and thus salt fingers are found in the regime:

$$0.64 \leq R_\rho \leq 1. \quad (18a)$$

Below  $R_\rho(\text{cr})$ , mixing is sustained primarily by shear. To determine  $R_\rho(\text{cr})$ , we consider the zero shear limit of Eq. (16c),  $2x^{-1} = S_s R_\rho - S_h$ . Using the  $S_{s,h}$  from (13b,c), a series of algebraic steps yields the simple equation:

$$A + Bx^{-1} - x^{-2} = 0 \quad (18b)$$

$$\begin{aligned} \frac{15}{7}A &= \pi_1(\mu - \pi_2 \pi_4) R_\rho - \pi_4(\eta + \pi_1 \pi_2 R_\rho) \\ &\quad - \frac{15}{7}(\eta \mu + \pi_1 \pi_2^2 \pi_4 R_\rho) \end{aligned}$$

$$\frac{15}{7}B = \pi_1 R_\rho - \pi_4 - \frac{15}{7}(\eta + \mu),$$

$$\eta \equiv \pi_1(\pi_2 - \pi_3 R_\rho),$$

$$\mu \equiv \pi_4(\pi_5 - \pi_2 R_\rho). \quad (18c)$$

Since  $R_\rho(\text{cr})$  corresponds to zero turbulent kinetic energy,  $E \rightarrow 0$  or  $x \rightarrow \infty$ , Eq. (18b) becomes  $A = 0$  which in turn gives

$$R_\rho(\text{cr}) = \pi_2^{-1} \delta^{-1} [1 \pm (1 - \pi_2^2 \delta^2 \xi)^{1/2}]$$

$$\delta = 2 \left( 1 + \frac{15}{7} \pi_3 \right) \left( \pi_5 + \pi_3 - 2\pi_2 + \frac{15}{7} \pi_3 \pi_5 \right)^{-1}$$

$$\xi = \left( 1 + \frac{15}{7} \pi_5 \right) \left( 1 + \frac{15}{7} \pi_3 \right)^{-1}. \quad (18d)$$

## 6. The dissipative timescales $\pi$

### a. General expressions

It is known that the RSM is unable to determine the dissipative timescales  $\pi$ . This is because the RSM does not provide the spectra of the different turbulence variables but only their integral over all wavenumbers while the determination of the dissipation timescales requires the spectra. In most geophysical applications (Mellor and Yamada 1982), the  $\pi$  were considered adjustable parameters and data were used to quantify them. In the presence of salt, there are three additional timescales  $\tau_{ps}$ ,  $\tau_{s\theta}$ , and  $\tau_s$  and the data may not be sufficient to determine all the  $\pi$ 's. In addition, even if one could fix a set of  $\pi$ 's, there is no guarantee that they would apply in circumstances different from those used for their determination. We shall therefore attempt to evaluate the  $\pi$ 's. Since  $(k^2 \kappa_T)^{-1}$  is the thermal timescale of an eddy of size  $k^{-1}$ , one has in general (Monin and Yaglom 1971, 1975):

$$\tau_{\theta}^{-1} = 2\kappa_T \left( \int k^2 E_T(k) dk \right) (\overline{T''^2})^{-1},$$

$$\frac{1}{2} \overline{T''^2} \equiv \int E_T(k) dk, \tag{19a}$$

where  $E_T(k)$  is the spectrum of the temperature variance. Analogous expressions hold true for salt with the changes  $\kappa_T \rightarrow \kappa_s$ ,  $E_T(k) \rightarrow E_s(k)$ ,  $T'' \rightarrow s''$ . As for the definition of  $\tau_{p\theta}$ , it is arrived at after integrating the two-point closure dynamic equations for the spectrum  $J(k)$  so that  $J_h = \int J(k) dk$ . A rather long derivation (Canuto and Dubovikov 1996a,b; 1997, hereafter CD) leads to the following results ( $\nu$  is the molecular viscosity):

$$\tau_{p\theta}^{-1} = \left[ \int k^2 (\nu_d + \chi_d) J(k) dk \right] J_h^{-1} \tag{19b}$$

$$\nu_d(k) = \left( \nu^2 + \frac{2}{5} \int_k^\infty p^{-2} E(p) dp \right)^{1/2} \tag{19c}$$

$$b\chi_d - \nu_d = (b\kappa_T - \nu) \left( \frac{a\kappa_T + \nu}{a\chi_d + \nu_d} \right)^{ab}. \tag{19d}$$

Here  $\nu_d(k)$  and  $\chi_d(k)$  are the dynamical or eddy, viscosity, and conductivity, which depend on the wave-number  $k$ . Relations (19b–d) are valid for any  $\nu$  and  $\kappa_T$ . Since the derivation of relations (19b–d) and of the coefficients  $a = 0.42$  and  $b = 0.72$  is rather involved (CD96–97) and cannot be repeated here, we shall try to give a physical interpretation. We begin with (19a) and the corresponding one for salt. The molecular diffusivity  $\kappa_T$  is independent of the size of the eddy  $\sim k^{-1}$  and is therefore outside the integral. On the other hand, as already discussed after Eq. (17c),  $\tau_{p\theta}$  is contributed by both molecular and pressure correlations. The latter become part of the nonlinear interactions whose closure brings about an “enhanced” eddy viscosity  $\nu_d$  and conductivity  $\chi_d$ . Since the latter are the sum of a turbulent part (from the nonlinear interactions) plus a molecular part, they are called dynamical (thus the subscript  $d$ ). Contrary to their molecular counterparts, dynamical diffusivities depend on the eddy size  $k^{-1}$ , and therefore are inside the integral.

As for Eq. (19c), the smaller the eddy (the larger the  $k$ ), the smaller is the integral and the more  $\nu_d(k) \rightarrow \nu$ , as indeed expected for small eddies. Equation (19c) entails the turbulent kinetic energy spectrum given by Kolmogorov law  $E(k) = Ko\epsilon^{2/3}k^{-5/3}$ , where  $1.5 \leq Ko \leq 1.8$ . A physical interpretation of (19c) is as follows. Consider the Reynolds number  $Re = UL\nu^{-1}$ . Using  $U \sim E^{1/2}$  and the size of the largest eddy  $L \sim k_0^{-1}$ , we also have  $Re \sim E^{1/2}k_0^{-1}\nu^{-1}$  and  $Re^2 \sim Ek_0^{-2}\nu^{-2}$ . Consider now a spectral Reynolds number squared  $Re_*^2(k)$  defined as

$$Re_*^2(k) = E(k)k^{-2}\nu^{-2},$$

$$Re^2(k) \equiv \int_k^\infty Re_*^2(p) dp. \tag{19e}$$

This allows us to rewrite (19c) in a more transparent form (we neglect numerical factors)

$$\nu_d(k) = \nu [1 + Re^2(k)]^{1/2}. \tag{19f}$$

When  $Re$  is small, the eddy viscosity reduces to the molecular  $\nu$ ; when the flow is very turbulent and  $Re > 1$ ,  $\nu_d$  is considerably larger than  $\nu$ . Next, consider Eq. (19d) that yields the dynamical (eddy) conductivity  $\chi_d(k)$  once the dynamical viscosity is known from (19c). Equation (19d) encompasses two limiting cases that previously had been treated separately. When molecular effects are negligible, Eq. (19d) gives  $\chi_d = b^{-1}\nu_d$ . In the opposite case, Eq. (19c) yields  $\nu_d \rightarrow \nu$  and substitution in (19d) shows that  $\chi_d = \kappa_T$ . Finally, we remark that the  $k$  integrations in Eqs. (19b,c) extend up to the dissipation wave scale  $\lambda_d = (\nu^3\epsilon^{-1})^{1/4}$  and that the ratio  $L/\lambda_d$  depends on  $Re$  because of the (model independent) relation  $L/\lambda_d = Re^{3/4}$ . The larger  $Re$ , the larger the ratio  $L/\lambda_d$  and the wider is the interval over which one must integrate the spectra. As the above relations indicate, to proceed one needs to know the various spectra, a topic that we discuss next.

*b. Weak turbulence*

In a low  $Re$  regime  $L/\lambda_d \sim O(1)$ , and the spectra are so narrow as to be almost delta functions,  $E(k) = E\delta(k - k_0)$ , which is Prandtl’s mixing length model where one large eddy prevails. Equations (19) and the ones for salinity, then yield (Zeman and Lumley 1982, 1983):

$$\pi_1 \equiv \tau_{ps}/\tau = (1 + \kappa_s\nu^{-1})^{-1},$$

$$\pi_2 \equiv \tau_{s\theta}/\tau = \nu(\kappa_s + \kappa_T)^{-1},$$

$$\pi_3 \equiv \tau_s/\tau = \nu\kappa_s^{-1},$$

$$\pi_4 \equiv \tau_{p\theta}/\tau = (1 + \kappa_T\nu^{-1})^{-1},$$

$$\pi_5 \equiv \tau_\theta/\tau = \nu/\kappa_T. \tag{20a}$$

The appearance of  $\nu$  is due to the fact that  $\tau = 2E/\epsilon$  where by definition  $\epsilon = 2\nu \int k^2 E(k) dk$ . Use of (20a) in (17b) gives

$$\frac{K_h}{K_s} \sim \frac{\kappa_T}{\kappa_s} \sim O(10^2) \tag{20b}$$

as expected. However, with Eq. (20a), Eq. (18d) has only one admissible root:

$$R_p(\text{cr}) = \frac{\kappa_s}{\kappa_T} \sim 10^{-2}, \quad 10^{-2} \leq R_p \leq 1. \tag{20c}$$

Weak turbulence allows a salt finger range much wider than what is observed [Eq. (18a)].

*c. Strong turbulence*

Next, we consider a regime opposite to the one in section 6b, namely when molecular effects are negligible. In such a case, we must have

$$\tau_\theta = \tau_s, \quad \tau_{ps} = \tau_{p\theta}, \quad (21a)$$

which considerably reduces the problem. To discuss  $\tau_{s\theta}$ , consider the correlation  $C$ :

$$C = \overline{T''s''}(\overline{T''^2})^{-1/2}(\overline{s''^2})^{-1/2}. \quad (21b)$$

Using Eqs. (8), (9), and (11), Eq. (21b) can be rewritten as

$$\tau_{s\theta} = \tau_s(K_s/K_h)^{1/2}(1 + K_s/K_h)^{-1}C. \quad (21c)$$

Using (21c) in (17a), the latter becomes a quadratic equation in  $(K_h/K_s)^{1/2}$  with only one physical root. Since the maximum value of  $C$  is unity, such solution is  $K_h = K_s$ . This is better than (20c) but still not correct since the NATRE data show that  $K_s = 1.6K_h$ . Furthermore, once  $K_s = K_h$  is substituted in (21c) and (18d), it gives

$$\tau_{s\theta}(\max) = \frac{1}{2}\tau_s, \quad R_\rho(\text{cr}) = 1. \quad (21d)$$

Contrary to the weak turbulence case (20c) that allows too wide a margin for salt fingers, this model has the opposite problem, it allows salt fingers only for  $R_\rho = 1$ , which contradicts (18a). Thus, even if we know how to compute  $\tau_\theta$  and  $\tau_{p\theta}$ , we could not use (21d) and we must search for a new model for  $\tau_{s\theta}$ .

*d. Moderate turbulence*

Since we do not have a theory capable of encompassing both weak and strong regimes, we must search for a compromise. We suggest the following: we adopt (21a) even in the case of moderate turbulence but not (21d), which we discuss last. To determine  $\tau_\theta$  and  $\tau_{p\theta}$ , we proceed as follows. Using the  $T$ -variance spectrum  $E_T(k) = \text{Ba}\epsilon^{-1/3}\chi_7k^{-5/3}$ , where Ba is the Batchelor constant, Eq. (19a) gives

$$\frac{\tau_\theta}{\tau} = \frac{\text{Ba}}{\text{Ko}} = \sigma_t = 0.72, \quad (22a)$$

where we have used  $\tau = 3\text{Ko}(k_0^2\epsilon)^{-1/3}$ . Next, in the limit of strong turbulence and with a Kolmogorov spectrum for  $E(k)$ , Eq. (19c) gives  $\nu_d(k) = (3/20\text{Ko}^3)^{1/2}\epsilon^{1/3}k^{-4/3}$ . In the strong limit, Eq. (19d) gives  $\chi_d = b^{-1}\nu_d$ . If we use the spectrum  $J(k) \sim k^{-n}$  with  $n = 7/3$ , as suggested by numerical simulations and two-point closure models (CD97), Eq. (19b) then yields

$$\frac{\tau}{\tau_{p\theta}} = \left(\frac{27}{5}\text{Ko}^3\right)^{1/2}(1 + \sigma_t^{-1}), \quad \sigma_t = b = 0.72. \quad (22b)$$

Thus, we have determined four of the needed timescales. As for  $\pi_2(\equiv\tau_{s\theta}/\tau)$ , we use (21a) in Eq. (18d) but treat  $\pi_2$  as a free variable. In Fig. 1 we plot  $R_\rho(\text{cr})$  versus  $\pi_2$ . One branch corresponds to salt finger while the symmetric one corresponds to diffusive convection. One can see that for a range of salt fingers to exist,  $\tau_{s\theta} < \tau_{s\theta}(\max)$ . In particular, if we decrease  $\pi_2$  by 10%,  $\tau_{s\theta}(\max)/\tau = \frac{1}{2}\tau_s/\tau = 0.36$ , to  $\tau_{s\theta}/\tau = 1/3$ , we obtain

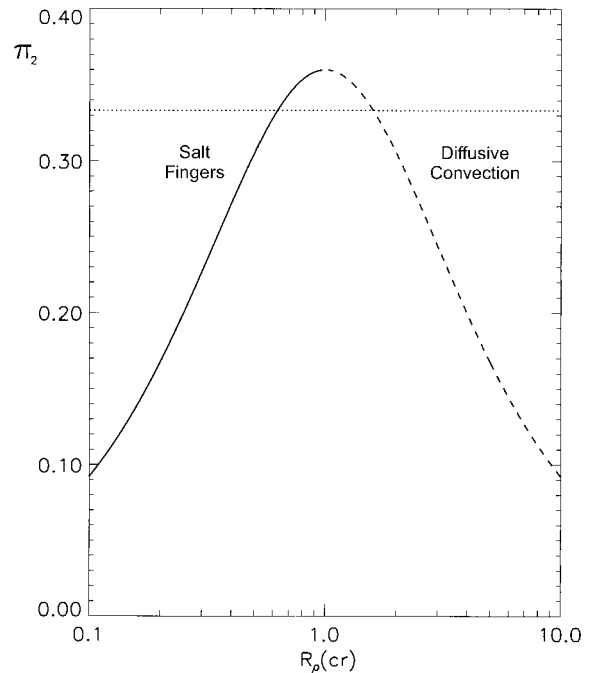


FIG. 1. The function  $R_\rho(\text{cr})$  given by Eqs. (18d) with  $\pi_2 = \tau_{s\theta}/\tau$  treated as a free variable. The full line corresponds to salt fingers while the dashed line corresponds to diffusive convection. If we take  $\pi_2 = 1/3$  (dotted line), for the case of salt fingers  $R_\rho(\text{cr}) = 0.62$ , Eq. (22c), while for diffusive-convection  $R_\rho(\text{cr}) = (0.62)^{-1}$ .

$$R_\rho(\text{cr}) = 0.62, \quad 0.62 \leq R_\rho \leq 1, \quad (22c)$$

which is close to (18a). The complete model for the  $\pi_s$  is therefore

$$\pi_1 = \frac{\tau_{ps}}{\tau} = \pi_4 = \frac{\tau_{p\theta}}{\tau} = \left(\frac{27}{5}\text{Ko}^3\right)^{-1/2}(1 + \sigma_t^{-1})^{-1},$$

$$\pi_2 = \frac{\tau_{s\theta}}{\tau} = \frac{1}{3}$$

$$\pi_3 = \frac{\tau_s}{\tau} = \pi_5 = \frac{\tau_\theta}{\tau} = \sigma_t = 0.72. \quad (22d)$$

**7. The critical Ri**

In analogy with  $R_\rho(\text{cr})$ , there is also an  $\text{Ri}^T(\text{cr})$  above which the effect of stable stratification is stronger than the mixing due to shear. As discussed in Part I, when  $R_\rho = 0$  we have  $\text{Ri}^T(\text{cr}) \sim O(1)$ . How is  $\text{Ri}^T(\text{cr})$  affected by  $R_\rho \neq 0$ ? Since SF and DC add destabilizing agents, one expects that, in the presence of double diffusion,  $\text{Ri}^T(\text{cr})$  is larger than without it. As in the case of  $R_\rho(\text{cr})$ , we obtain  $\text{Ri}^T(\text{cr})$  by taking the  $E \rightarrow 0$  limit of (16c). The problem can be treated analytically. Substituting the expressions for  $S_{h,s}$  from (13b,c), a relatively lengthy algebra leads to the following result:

$$\text{Ri}^T(\text{cr}) = f(R_\rho). \quad (23a)$$

The explicit form of the function  $f(R_\rho)$  is given in ap-

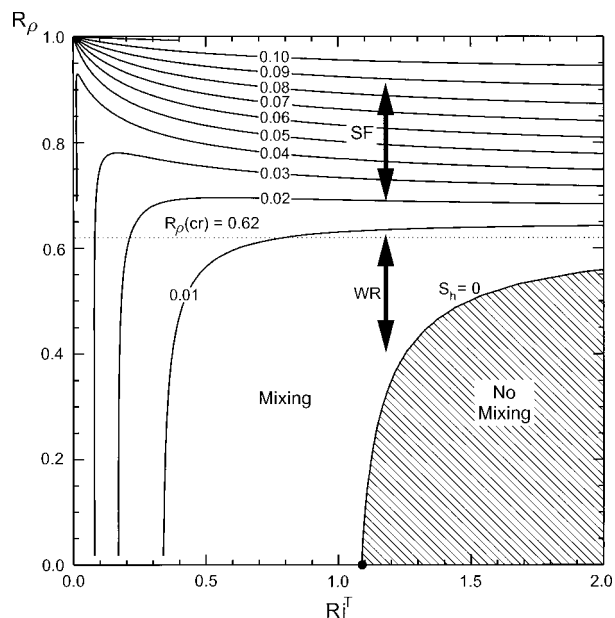


FIG. 2. Contour plots of the stability function  $S_h$ , Eq. (13b), in the  $Ri^T$ - $R_\rho$  plane. The zero contour  $S_h = 0$  yields  $Ri^T(cr)$  above which mixing is no longer present [the values correspond to Eq. (23a) and appendix C]. The value of  $R_\rho(cr)$  is also shown.

pendix C. The result is shown in Fig. 2 where we plot iso-contours of  $S_h$  beginning with  $S_h = 0$  below which there is “no mixing”; that is, the  $S_h = 0$  curve depicts the function

$$Ri^T(cr) \equiv N^2 \Sigma^{-2} |_{cr}. \quad (23b)$$

In the absence of double diffusion  $R_\rho = 0$ , one observes that  $Ri^T(cr) \approx 1$ , as suggested by Munk (1966). In the presence of double-diffusion and when  $R_\rho$  is positive, the value of  $Ri^T(cr)$  increases rather slowly at first with  $R_\rho$  and then steepens, the asymptote occurring at  $R_\rho(cr) = 0.62$ . Since mixing is now enhanced by double diffusion, the overall mixing lives longer, the maximum extent being given by the value of  $Ri^T(cr)$ . An interesting feature of Fig. 2 is the difference that occurs above and below  $R_\rho(cr)$ . In the upper curves, where  $R_\rho > R_\rho(cr)$ , at fixed  $R_\rho$ , in going from right (small shear) to left (large shear) on the horizontal axis, the diffusivities ( $S_h$ ) decrease as shear increases. In the lower region, where  $R_\rho < R_\rho(cr)$ , at a fixed  $R_\rho$ , the opposite occurs, in going from right to left, the diffusivities increase as the shear increases. In the last case, when shear is “constructive,” mixing is governed mostly by a wave regime (symbol WR) rather than by double diffusion (SF for salt fingers). In the WR regime, we follow Munk’s (1966, 1981) suggestion that “the internal wave shear is associated with Richardson numbers of order unity,”  $Ri^T \sim Ri^T(cr) \sim O(1)$ . However, because of double diffusion,  $Ri^T(cr)$  is no longer a constant but a function of  $R_\rho$ . We shall therefore take

$$Ri^T = c Ri^T(cr) = cf(R_\rho), \quad (23c)$$

where  $c$  is a constant of order unity. The sensitivity of the results to the parameter  $c$  is exhibited in Fig. 7b.

### 8. Internal wave field

Below the ML, the shear generated by the external wind is too weak to generate the observed mixing (Ledwell et al. 1993, 1998). On the other hand, a random superposition of internal waves may give rise to a finite probability that local values of  $Ri$  fall well below the critical value, for example,  $Ri^T < 1/4$  (Desaubies and Smith 1982). Nonlinear wave interactions have been extensively studied (McComas and Müller 1981; Henyey et al. 1986; Moun and Osborn 1986; Gregg 1989; Polzin et al. 1995; Kunze and Sanford 1996; Gregg et al. 1996; Polzin 1996; Toole 1998; Sun and Kunze 1999a,b; D’Asaro and Lien 2000a,b). In particular, Polzin (1996) has analyzed the dissipation rate  $\epsilon$  resulting from NATRE data and concluded that the WKB model of Kunze et al. (1990) provides an “effective parameterization of  $\epsilon$  for a broad range of variability in the background.” However, since OGCM do not resolve the pertinent scales, such a model cannot be employed here. Analyzing several of the suggested models for the  $\epsilon$  versus  $N$  relations, Polzin et al. (1995) concluded that the scaling  $\epsilon \sim N^{3/2}$  is not consistent with the data while  $\epsilon \sim N^2$  is (their Fig. 4). Using Sargasso Sea data, Kunze and Sanford (1996, KS96) suggest what they call the Gregg–Henyey–Polzin parameterization (cgs units,  $A$  is dimensionless):

$$\frac{\epsilon}{N^2} = 0.288A, \quad A \equiv \frac{\langle V_z^2 \rangle^2}{\langle V_z^2 \rangle_{GM}^2} f(R_\omega), \quad (23d)$$

$$R_\omega = \langle V_z^2 \rangle N^{-2} \xi_z^{-2}.$$

Here,  $\langle V_z^2 \rangle$  is the shear variance referred to the GM background (Garrett and Munk 1975, hereafter GM) and  $R_\omega$  is the shear to strain ( $\xi_z$ ) ratio which for GM is 3. The explicit form of  $f(R_\omega)$  is given by Eq. (5) of KS96 where Fig. 5 shows that over the entire depth of the ocean, even with  $f(R_\omega) = 1$ ,  $A$  varies at most by a factor of  $\sim 2$  in the stratified interior (Polzin et al. 1995; Kunze and Sanford 1996; Gregg et al. 1996; Polzin 1996; Toole 1998).

However, near rough topography,  $A$  changes by two to three orders of magnitude (Polzin et al. 1997; Kunze and Toole 1997). Thus, through the presence of  $\epsilon$ , the present model can account for the different stirring mechanisms that occur in different parts of the ocean, a flexibility that is required for there is no universal stirring mechanism. Moreover, since the diffusivities depend on the efficiency  $\Gamma_\alpha$ , which are also not constant, one needs a turbulence model to compute them.

### 9. The full model

The fluxes entering Eqs. (2a–c) for the resolved fields are given by Eqs. (2d) and the diffusivities  $K_\alpha$  are given



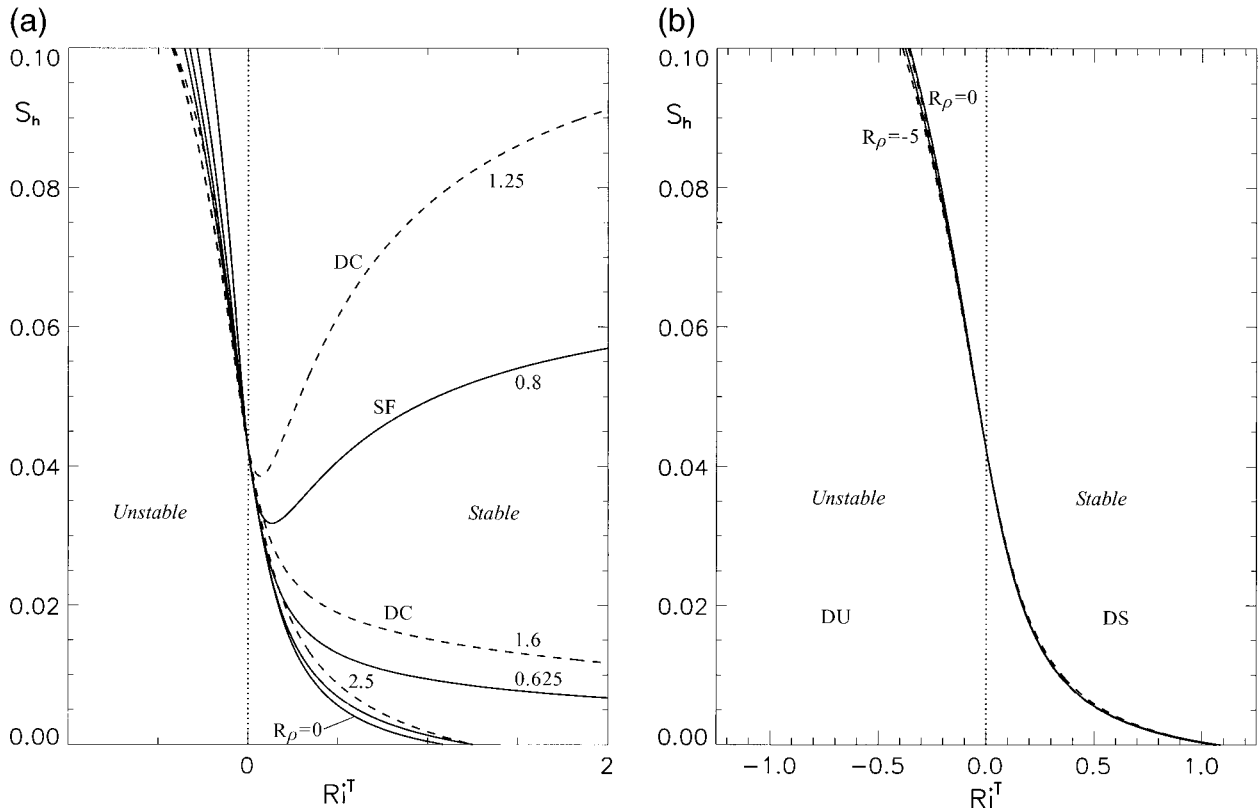


FIG. 3. (a) The dimensionless stability function  $S_h$  for heat diffusivity, Eq. (13b), vs stable  $Ri^T$  for different values of  $R_\rho$ . Local model, Eq. (16c). Salt fingers (solid line). Diffusive convection (dashed line). We recall that  $Ri^T > 0$  corresponds to dynamical stability while  $Ri^T < 0$  corresponds to dynamical instability. (b) As in (a) but for the DU and DS cases [see definitions after Eq. (4b)]. The values  $R_\rho = 0, -0.2, -1, -5$  yield nearly identical results.

by Eqs. (4b). The structure functions  $S_\alpha$  are given by Eqs. (13)–(15) and the variable  $(\tau N)^2$  is obtained by solving the algebraic relation (16c). The dimensionless variables  $y$ ,  $n$ , and  $c$  entering the  $S_\alpha$  are then known functions of the large-scale fields. The above procedure is valid both in the ML and below it. As for the dissipation  $\epsilon$ , one must use different treatments in the ML and below it.

The distinction between the two regimes is made on the basis of the value of  $Ri^T(\text{resolved}) \equiv N^2 \Sigma^{-2}$  [see Eq. (3a)]. We use the ML model when  $Ri^T(\text{resolved}) \leq Ri^T(\text{cr})$ . Since the latter is  $\geq 1$ , what is referred to as ML actually includes part of the upper thermocline.

#### a. Mixed layer

One may adopt the Kolmogorov-type law

$$\epsilon = E^{3/2} \Lambda^{-1} = 8 \Lambda^2 \tau^{-3}, \quad (24a)$$

where  $\tau$  is given by solving (16c). Equation (24a) requires a model for the length scale  $\Lambda$ . Using a two-point closure Cheng and Canuto (1994, CC94) derived an expression for  $\Lambda$  [Eqs. (38) of CC94], which we found to be well represented by the empirical relations (Blackadar 1962; Deardorff 1980):

$$\Lambda = 2^{-3/2} B_1 l, \quad l = \min\left(\frac{1}{2} \frac{q}{N}, l_1\right),$$

$$l_1 = \kappa z l_0 (l_0 + \kappa z)^{-1}, \quad (24b)$$

which are easier to employ than Eq. (38) of CC94. Here,  $\frac{1}{2} q^2 = E$ ,  $\kappa = 0.4$  is the von Kármán constant and  $B_1 = 16.6$ . In the present case  $l_0 = 0.17H$ , where  $H$  is the mixed layer depth determined by the relation  $g[\rho(H) - \rho(\text{surface})]\rho(H)^{-1} = 3 \times 10^{-4} \text{ m s}^{-2}$ . Other authors (Burchard and Bolding 2001) have employed a differential equation for  $\epsilon$ .

#### b. Below the mixed layer

On the one hand, Eq. (24a) does not seem appropriate because it is hard to define a meaningful mixing length  $\Lambda$ , while on the other hand use of a differential equation for  $\epsilon$  led to underpredicting  $\epsilon$  (Burchard et al. 1998), a situation that was remedied by a cutoff in  $E$ . D'Asaro and Lien (2000a,b) point out that there is a more basic conceptual problem since the  $E$  and  $\epsilon$  equations, especially the latter, do not naturally account for a basic ingredient of stably stratified flows, the existence of internal waves. Since we arrived at the same conclusion,

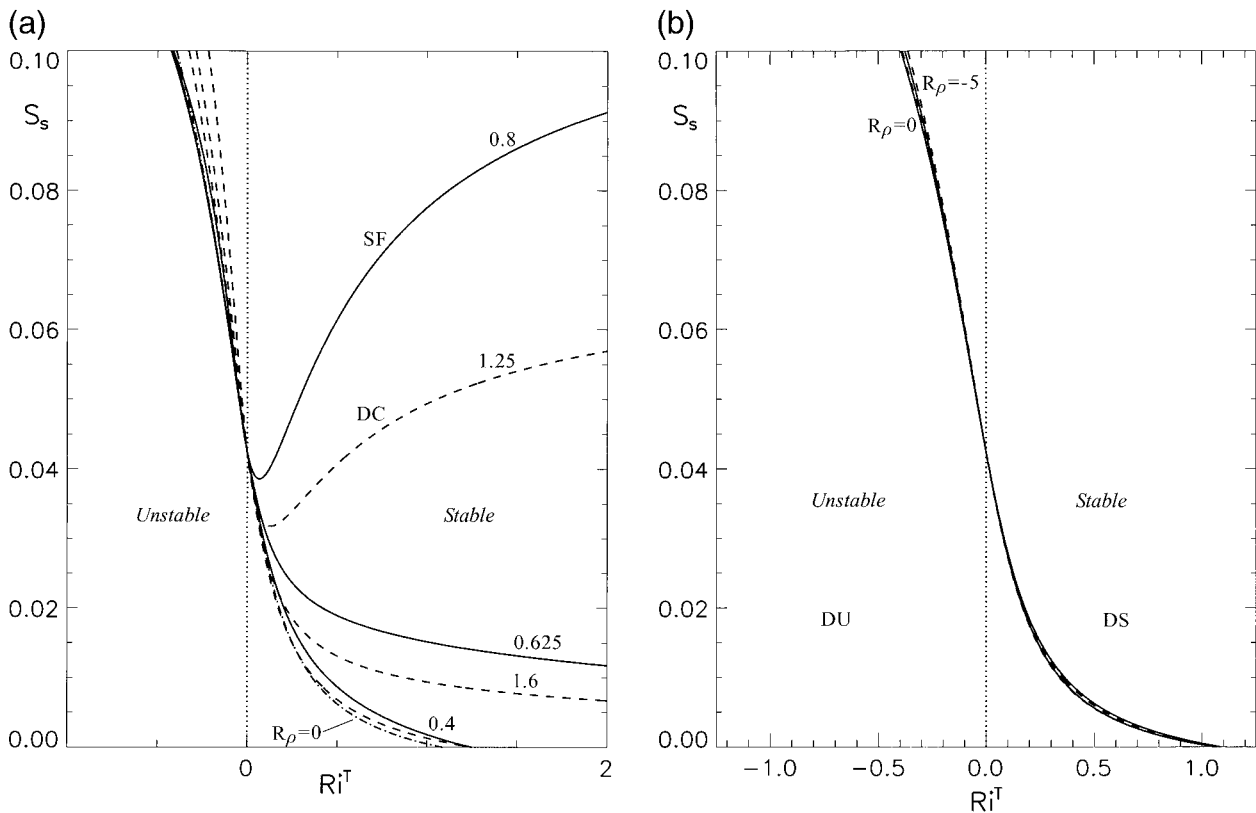


FIG. 4. (a) Same as in Fig. 3a but for the salinity stability function  $S_s$ , Eq. (13c). Note that the curves for the SF and DC cases have exchanged places as compared with Fig. 3a. (b) As in (a) but for the DU and DS cases [see definitions after Eq. (4b)].

we decided to consider  $\epsilon$  as an input function that may be due to internal waves or to more complex processes, as discussed in section 8.

**10. Comparison with previous models**

Since the Osborn–Cox (1972) and the Osborn (1980) models (called OC models) have been widely used to translate measurements into diffusivities (Davis 1994a,b), it is important to compare ours with the OC models. The most distinguishing features are 1) the OC models employ production equals dissipation, as we do; 2) the OC models were not intended to describe double diffusive processes, which are the primary subject of this paper; 3) the OC models do not compute the mixing efficiencies  $\Gamma$ , which are assigned values around 0.2 as indicated by a variety of data, whereas this model computes them.

To make the comparison physically transparent, consider the mass diffusivity  $K_\rho$ , Eq. (3d). It can be written as ( $R_f$  is the flux Richardson number):

$$K_\rho = \Gamma_\rho \epsilon N^{-2}, \quad \Gamma_\rho = R_f(1 - R_f)^{-1},$$

$$R_f \equiv (K_\rho/K_m) Ri^T. \tag{24c}$$

Next, if one writes the heat diffusivity as  $K_h = \kappa_T C_T$  (Gregg 1987), where  $C_T$  is the Cox number,  $\Gamma_\rho$  can be rewritten as

$$\Gamma_\rho = \kappa_T C_T N^2 \epsilon^{-1} (K_\rho/K_h). \tag{24d}$$

When  $K_\rho = K_h$ , Eq. (24d) becomes Gregg’s Eq. (49). Using (3e), we now have

$$\Gamma_\rho^{DD} = \Gamma_\rho^{OCG} (1 - K_s R_\rho / K_h) (1 - R_\rho)^{-1}, \tag{24e}$$

where DD and OCG stand for double diffusion and Osborn–Cox–Gregg. In salt fingers,  $K_s > K_h$  while in diffusive convection  $K_h > K_s$  so that we have the relations:

$$\text{SF: } \Gamma_\rho^{DD} < \Gamma_\rho^{OCG}, \quad \text{DC: } \Gamma_\rho^{OCG} < \Gamma_\rho^{DD}. \tag{24f}$$

The primary focus of most recent work has been to assess the relative contributions of turbulence and wave breaking (McDougall and Ruddick 1992; St. Laurent and Schmitt 1999). The latest model by Walsh and Ruddick (2000, WR00) can be formulated as

$$K_\alpha = K_\alpha(\text{SF}) + K_\alpha(t) \tag{25a}$$

$$K_h(\text{SF}) = \gamma_f K_s(\text{SF}) R_\rho, \quad K_h(t) = K_s(t), \tag{25b}$$

where  $\gamma_f$  is the heat-to-salt flux ratio and the letter  $t$  stands for turbulence. In Eq. (25b),  $\gamma_f$  is taken from the linear stability analysis (Stern 1975; Kunze 1987; Schmitt 1994) while turbulence yields identical heat and salt diffusivities.

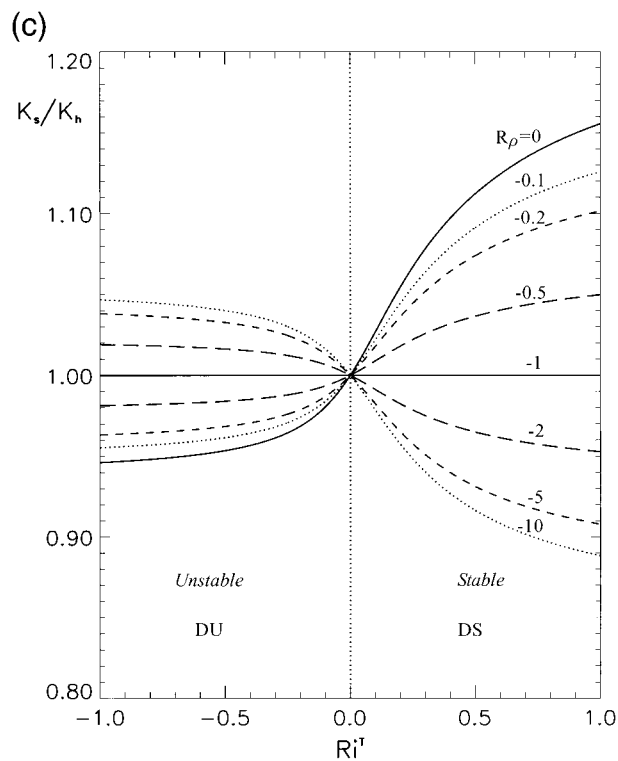
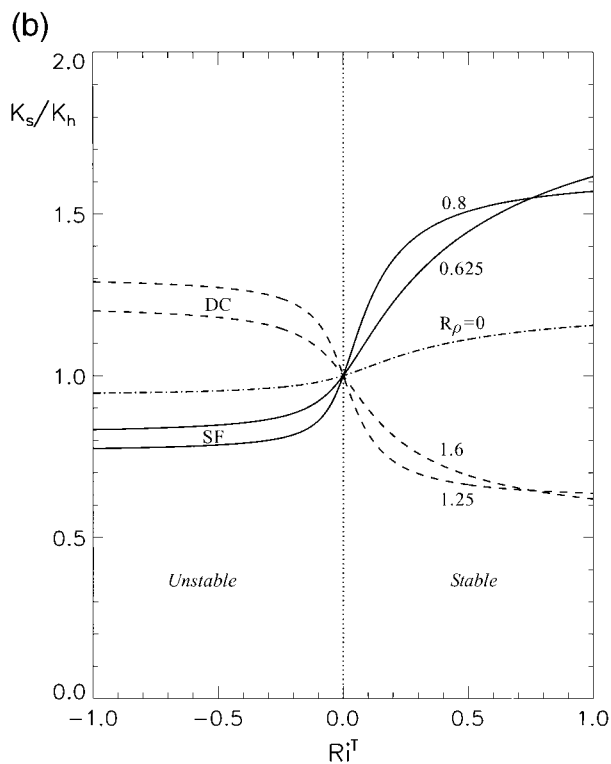
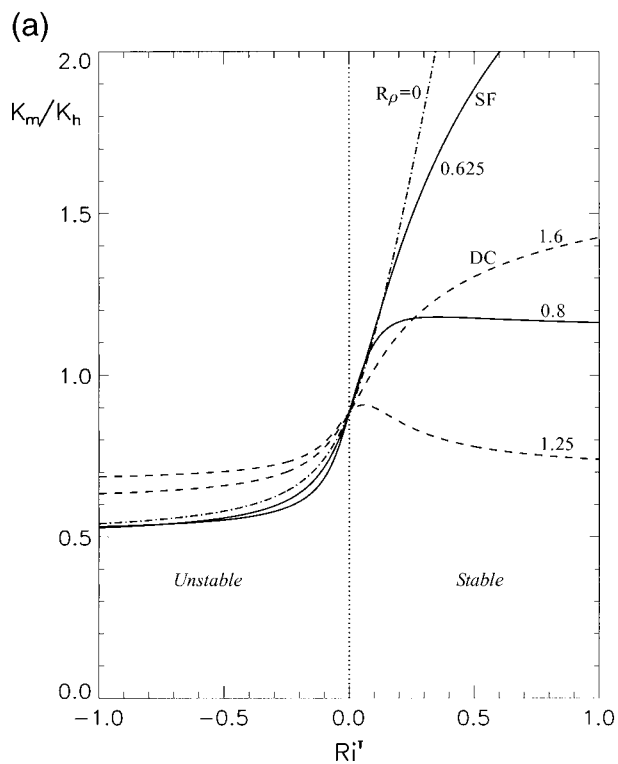


FIG. 5. (a: top left) The ratio  $K_m/K_h$  vs  $Ri^T$ ;  $R_\rho = 0$  corresponds to the laboratory data discussed in Part I. Salt fingers (solid line); diffusive convection (dashed line). (b: top right) The ratio  $K_s/K_h$  vs  $Ri^T$  for different  $R_\rho$ . Salt fingers (solid line). Diffusive convection (dashed line). (c: bottom left) The ratio  $K_s/K_h$  vs  $Ri^T$  for different  $R_\rho$ . Cases DU and DS [see definitions after Eq. (4b)].

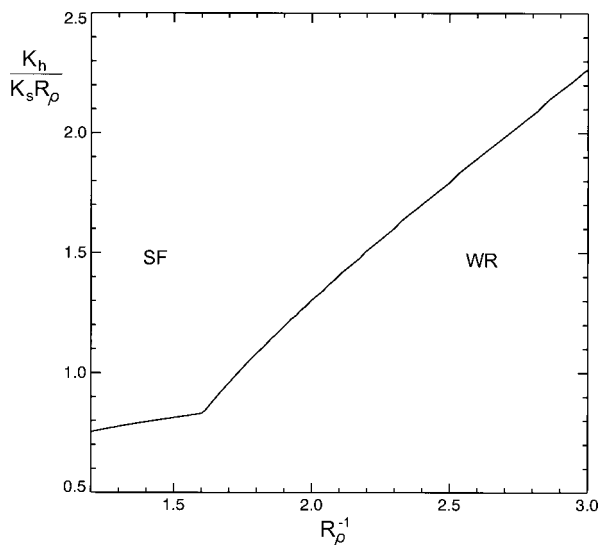


FIG. 6. The heat-to-salt flux ratio  $(K_h/K_s)R_\rho^{-1}$  vs  $R_\rho^{-1}$ . In the SF region, we have taken  $Ri^T$  very large while in the WR (wave-dominated region),  $Ri^T$  is computed using (23c). This result compares well with Fig. 2 of Walsh and Ruddick (2000).

In terms of the model presented in this paper, Eqs. (25) are equivalent to summing the weak and the strong turbulence models discussed earlier. Our model does not impose such a separation and computes  $\gamma_f$  from the full nonlinear problem (Fig. 6). The rationale behind our model is to try to represent the effects of both processes (double diffusion and turbulence) averaged together over space and time. Our view is that, although locally and temporarily there are sometimes salt fingers growing in such a way as to approximate the weak turbulence model as well as laboratory experiments without shear and at other times a random superposition of internal waves may produce so strong a shear that the mixing is well described by a strong regime  $K_h = K_s$ , neither of these situations is either ubiquitous or permanent. Rather, fingers form and grow for a while but they are disrupted by temporary bursts of high shear that subside and allow the fingers to form and grow again, the two processes eventually reaching equilibrium. The diffusivities  $K_h$  and  $K_s$  produced by salt fingering, internal wave shear mixing, and the interaction of the two have spatial and temporal scales larger than those of the two separate processes. Whereas in the previous approaches (St. Laurent and Schmitt 1999; Walsh and Ruddick 2000), the prevalence of salt fingers versus strong turbulence must be computed at each point from the microstructure data, our approach (intended for use in OGCMs where such small-scale information is not available), determines the balance between salt fingering and shear mixing using the large-scale  $R_\rho$ . The variation in the relative strengths of the two phenomena at different locations is attributed to the variation in  $R_\rho$ .

As for the implementation in OGCM, three approaches were used to treat mixing below the ML. One treats

the  $K_\alpha$  as adjustable background diffusivities, for example in the NCAR OGCM (Large et al. 1997)  $K_m = 16.7 \text{ cm}^2 \text{ s}^{-1}$  and  $K_s = K_h = 0.5 \text{ cm}^2 \text{ s}^{-1}$  while other authors (e.g., Merryfield et al. 1999) use a different set of values. It should be remarked that the above  $K_m$  is much larger than one provided by this model (Fig. 8) and so are the values of  $K_{h,s}$  compared with 0.07 of Polzin et al. (1995, Fig. 3), 0.1 of Kunze and Sanford (1996, Fig. 5), and the NATRE data (Figs. 9 and 10). Zhang et al. (1998, hereafter ZSH) and Merryfield et al. (1999, hereafter MGH) used model (25) for heat and salt in the form

$$K = K[R_\rho, R_\rho(\text{cr})] + K(\text{waves}). \quad (26a)$$

The first term was taken from the phenomenological models of Schmitt (1981), Fedorov (1988), and Kelley (1984, 1990) and  $R_\rho(\text{cr}) = 0.64$  (section 5). As for the second term in (26a), two models have been adopted both of which are independent of  $R_\rho$ :

$$K^{\text{ZSH}}(\text{waves}) = K_\infty = \text{const},$$

$$K^{\text{MHG}}(\text{waves}) = a_0 N^{-1}. \quad (26b)$$

In the present model the internal wave contribution depends on  $R_\rho$  since schematically

$$\begin{aligned} K(\text{waves}) &= K(Ri^T, R_\rho, \epsilon) = K(cRi_{\text{cr}}^T, R_\rho, \epsilon) \\ &= K(R_\rho, \epsilon). \end{aligned} \quad (26c)$$

### 11. Turbulent diffusivities: General properties

Figures 3–4 exhibit the dimensionless structure functions  $S_{h,s}$  versus stable  $Ri^T$  for salt fingers and diffusive convection. Consider first the case of salt fingers. At a fixed  $Ri^T$ , the structure function increases as  $R_\rho$  increases. This behavior is physically understandable since the instability is generated by salt and the stronger the source, the larger the diffusivity. Next, consider the dependence on  $Ri^T$  and in particular the value of  $Ri^T(\text{cr})$  above which turbulent mixing ceases to exist as indicated by the vanishing of the  $S$ 's. For  $R_\rho = 0$  (lowest curve, no salt instabilities),  $Ri^T(\text{cr}) \sim O(1)$ , as found in Part I. As salt instabilities begin to appear and  $R_\rho > 0$ , the value of  $Ri(\text{cr})$  becomes increasingly larger implying that turbulent mixing can exist longer than without salt instability processes. At  $R_\rho = R_\rho(\text{cr})$ , the value of  $Ri^T(\text{cr})$  become exceedingly large, see Fig. 2. For values of  $R_\rho > R_\rho(\text{cr})$ , there is no longer an  $Ri^T(\text{cr})$  since the structure functions no longer vanish for any  $Ri^T$ . This implies that even without shear  $Ri^T \rightarrow \infty$ , there is finite mixing due to the chaotic nature of the salt instabilities themselves. We notice that below  $R_\rho(\text{cr})$ , the larger the shear ( $Ri^T \rightarrow 0$ ), the larger the diffusivities. In other words, both salt and shear contribute to the instability. Above  $R_\rho(\text{cr})$ , the situation is reversed, the larger the shear ( $Ri^T \rightarrow 0$ ), the smaller the diffusivity, which implies that shear and salt fingers interfere. Next, consider the DC cases. At a given  $Ri^T$ , as  $R_\rho$  increases, the structure function decreases; just

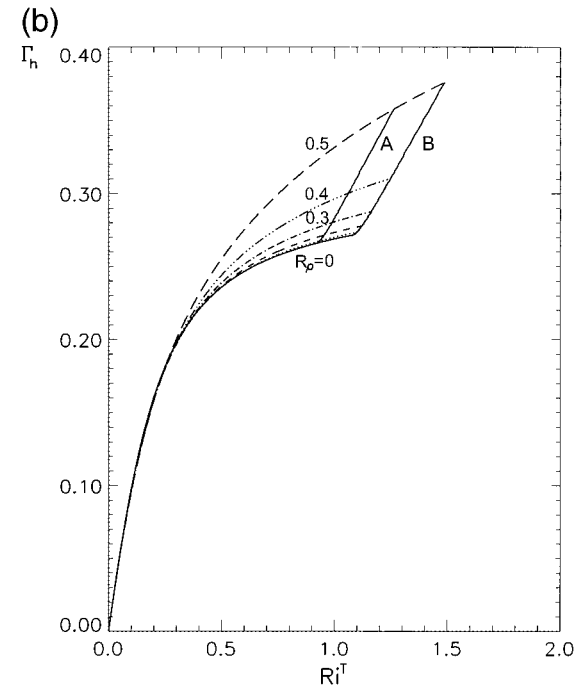
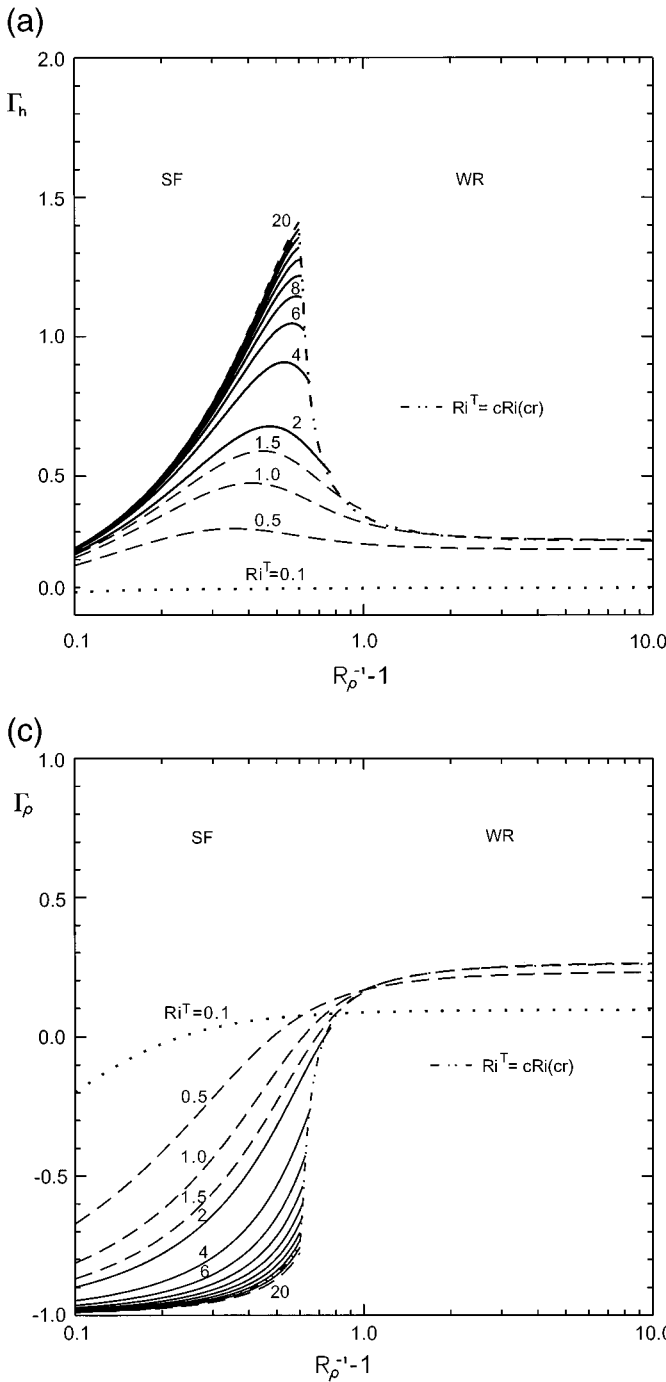


FIG. 7. (a: top left) The heat mixing efficiency  $\Gamma_h = K_h N^2 \epsilon^{-1}$  vs  $R_\rho^{-1} - 1$  for different stable  $Ri^T$ . Using NATRE data, St. Laurent and Schmitt (1999, Fig. 8) have suggested a way to interpret the dependence of  $\Gamma_h$  on  $Ri^T$ . Although it is not easy to make a one-to-one correspondence with their work, the general trend predicted by the model in the SF region agrees with the data: the smaller the shear, the larger the  $\Gamma_h$ . (b: top right) The heat mixing efficiency  $\Gamma_h = K_h N^2 \epsilon^{-1}$  vs stable  $Ri^T$  for different  $R_\rho$ . The two lines A and B correspond to  $c = 0.85$  and  $c = 1$ , where  $c$  is the parameter entering Eq. (23c). Since the curves bend over, their sensitivity to  $c$  decreases. For a given  $R_\rho$ , the effect of changing  $c$  on  $\Gamma_h$  is not large. In this paper,  $c = 0.85$ . (c: bottom left) The mass mixing efficiency  $\Gamma_\rho = K_\rho N^2 \epsilon^{-1}$  vs  $R_\rho^{-1} - 1$  for different stable  $Ri^T$ . In the WR regime a value  $\Gamma_\rho = 0.2$  is usually employed in the literature (Osborn and Cox 1972; Schmitt 1994; St. Laurent and Schmitt 1999). Here, it is derived within the model.

the opposite of the SF case. This is in accordance with the fact that in this case salt acts as a sink of mixing (which in turn is caused by an unstable temperature gradient), and thus, the stronger the sink, the lower the level of mixing, a circumstance that is reflected in the decrease of the diffusivity. As for the effect of shear, we notice that here too, above  $R_\rho(cr)$ , the larger the shear, the larger the diffusivities while the opposite occurs for values of  $R_\rho$  larger than that critical value. Finally, we recall that

$Ri^T > 0$  corresponds to dynamical stability while  $Ri^T < 0$  corresponds to dynamical instability. Understandably, the DS cases correspond to the lowest diffusivity because both salt and temperature gradients are stabilizing. The only source of instability is shear and thus turbulent mixing dies when stratification is too strong. In the DU side, the opposite occurs in the sense that both  $T$  and  $S$  are unstable and the resulting diffusivities are the largest. In Figs. 5a-c we plot the ratios  $K_m/K_h$  and  $K_s/K_h$ , which

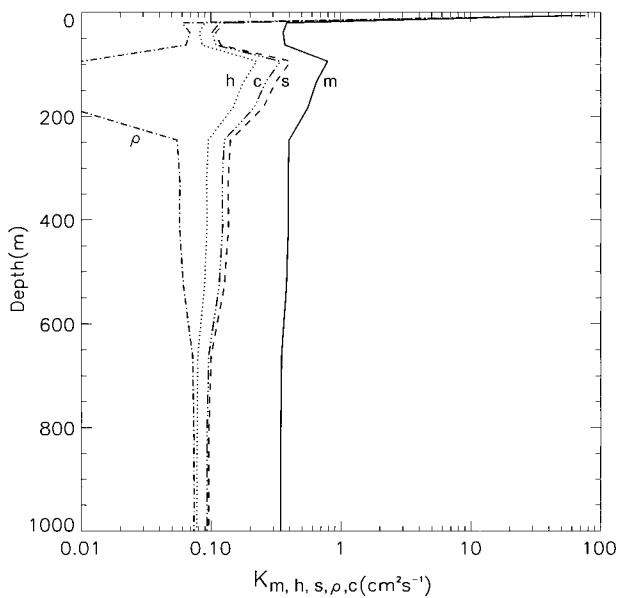


FIG. 8. The five diffusivities for momentum ( $m$ ), heat ( $h$ ), salt ( $s$ ), mass ( $\rho$ ), and passive scalar ( $c$ ) vs depth for the location corresponding to the NATRE measurements.

show that  $K_h$  and  $K_s$  are indeed different. In stable salt fingers, Fig. 5b,  $K_s$  is larger than  $K_h$  in accord with measured data.

The stable  $R_\rho = -1$  case shown in Fig. 5c has been studied with a 2D numerical simulation by Merryfield et al. (1998, Fig. 3b). The results of Fig. 5c are only valid in the regime  $Re \gg 1$  where they agree, as ex-

pected, with the 2D results (above the dotted lines in their fig. 3b). Intermediate values of  $Re$  correspond to a region in which molecular effects are still relevant and one must therefore employ Eqs. (20c) for the  $\pi$ 's. It is easy to see that the present model yields  $K_h/K_s = 4$  for  $Fr \approx 28$ , which agrees pretty well with the corresponding values in Fig. 3b of the 2D simulation (we recall that our  $x = 4Fr^{-2}$ ).

In Fig. 6 we plot the heat-to-salt flux ratio ( $K_h/K_s$ ) $R_\rho^{-1}$ . Since  $R_\rho(cr) = 0.62$  and since for  $R_\rho < R_\rho(cr)$ , we have a wave dominated regime (WR), while for  $R_\rho > R_\rho(cr)$  we have salt fingers (SF), we notice that in the SF region, the model results agree with the reported data (see Figs. 5b and 10 of St. Laurent and Schmitt 1999). In the wave region (WR), the presence of the additional mixing due to shear increases both  $K_h$  and  $K_s$ , making their ratio become closer to unity than in the SF regime. The behavior in Fig. 6 is in agreement with the model of Walsh and Ruddick (2000, Fig. 2).

In Fig. 7a we plot  $\Gamma_h = K_h N^2 \epsilon^{-1}$  versus  $R_\rho^{-1} - 1$  for different values of stable  $Ri^T$ . The lowest curve is for  $Ri^T = 0.1$ , while the upper curve is for  $Ri^T = 20$ . As expected from Fig. 2, in the SF regime ( $R_\rho > 0.62$ ), the larger the shear, the lower the value of  $\Gamma_h$ . The largest  $Ri^T$  curve corresponds to the points to the extreme right of Fig. 2 and the corresponding  $R_\rho(cr) = 0.62$ . As we consider increasingly smaller values of  $Ri^T$ , we are sliding down the dividing line in Fig. 2, which corresponds to smaller  $R_\rho(cr)$  and this moves the last point of the curves in Fig. 7a to the right. This general trend is in keeping with the NATRE results of Fig. 9 of St. Laurent and Schmitt (1999, hereafter SLS) where the smaller

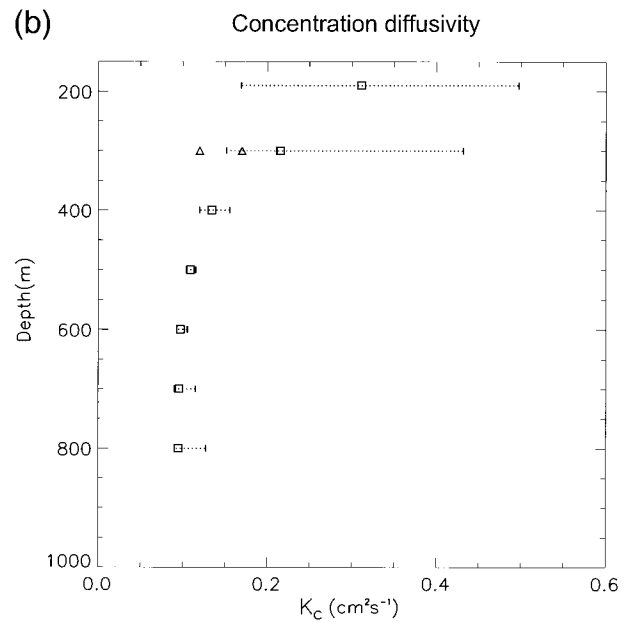
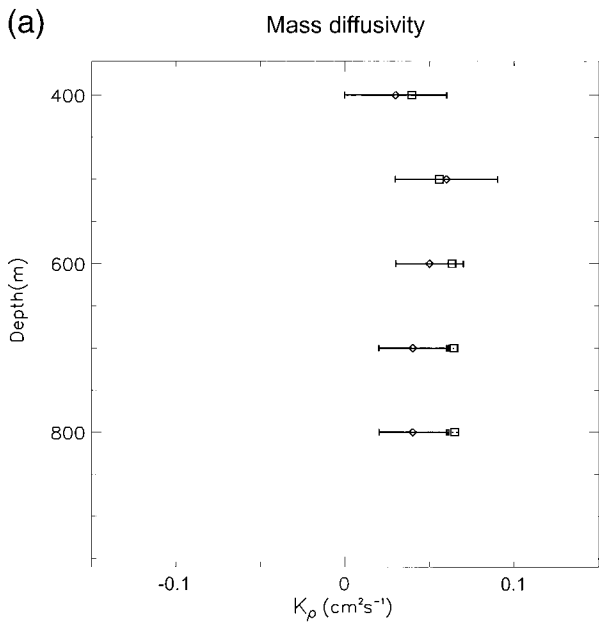


FIG. 9. (a) Testing the diffusivity model without an OGCM. Mass diffusivity  $K_\rho$  compared with NATRE data (diamonds with error bars; St. Laurent and Schmitt 1999). Model results are represented by squares with error bars. (b) Same as (a) but for the concentration diffusivity  $K_c$  [triangles from NATRE data from Ledwell et al. (1993, 1998)].

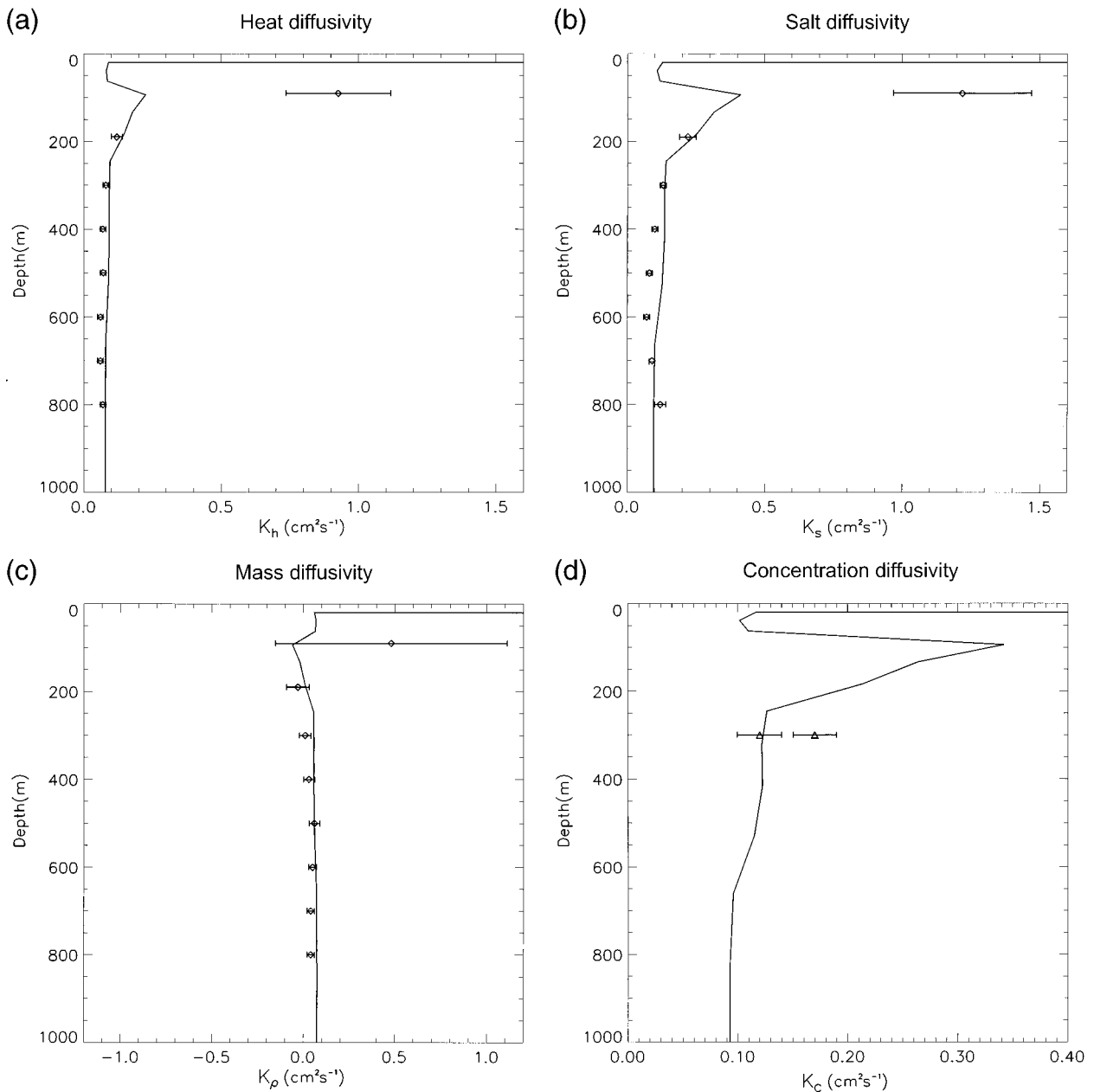


FIG. 10. Testing the diffusivity model with an OGCM. (a) Heat diffusivity  $K_h$  compared with NATRE data [diamonds with error bars from St. Laurent and Schmitt (1999)]. Model results are represented by a solid line. (b) As in (a) but for salt diffusivity  $K_s$ . (c) As in (a) but for mass diffusivity  $K_\rho$ . (d) As in (a) but for the concentration diffusivity  $K_c$  [triangles from NATRE data from Ledwell et al. (1993, 1998)].

the value of  $Ri^T$ , the wider the range of  $R_\rho$  allowed. In particular, from Fig. 9f of SLS we see that for  $Ri^T > 5$ , the range of allowed  $R_\rho$  is  $0.5 \leq R_\rho \leq 1$ , in agreement with both Figs. 2 and 7a. We also notice from Figs. 9a–f of SLS that the larger the  $Ri^T$ , the larger the  $\Gamma_h$ , a feature that is also reproduced in our Fig. 7a. In Fig. 7b we exhibit  $\Gamma_h$  versus stable  $Ri^T$  for different  $R_\rho$ . The two lines A and B correspond to different choices of  $c$  in Eq. (23c): A ( $c = 0.85$ ) and B ( $c = 1$ ). One can see that for a given  $R_\rho$ , the choice of  $c$  does not greatly

influence the resulting value of  $\Gamma_h$ . In Fig. 7c we exhibit  $\Gamma_\rho$  versus  $R_\rho$  for different stable  $Ri^T$ . The Osborn–Cox model employs  $\Gamma_\rho = 0.2$ , which the present model reproduces in the WR regime.

## 12. Testing the model without an OGCM

Though the ultimate goal is to employ the new diffusivities in an OGCM, it would be very helpful and less affected by the unavoidable complexities of any

OGCM, if one could use the NATRE data to test the model directly. This is indeed possible. In the deep ocean, the present model yields diffusivities (1b) that depend on  $R_\rho$ ,  $N$ , and  $\epsilon$ . Due to the location of the NATRE experiments,  $\epsilon$  can be modeled with (23d). Thus, the comparison with NATRE data can be carried out without running an OGCM: using  $R_\rho$  (data) in our model expressions, one obtains  $K_\alpha$  (model), which is then compared with  $K_\alpha$  (data). Some of the results are presented in Figs. 9a,b. We extracted the errors in  $R_\rho$  and  $K_h$  from St. Laurent and Schmitt (1999) and thus both data and model results are shown with error bars. The  $K_\alpha$  are sensitive to  $\pi_2$  and we verified that a slightly larger  $\pi_2$  would improve the agreement. The procedure faces a practical difficulty since NATRE data fall within a small interval of  $R_\rho$  that cluster around  $R_\rho(\text{cr})$ . As one can see from Fig. 7a, in this small interval  $\Gamma_h$  is a steep function of  $R_\rho$  and a small error in  $R_\rho$  can give quite different  $\Gamma_h$ .

**13. Testing the model with an OGCM**

We employed a 3D global ocean model, the NCAR CSM Ocean Model produced by the University Corporation for Research, National Center for Atmospheric Research, Climate and Global Dynamics Division. We used the stand-alone  $3^\circ \times 3^\circ$  configuration with 25 levels (Large et al. 1997). Details can be found in Part I.

In Figs. 10a–d, we present momentum, heat, salt, mass, and concentration diffusivities versus the NATRE data [diamonds from SLS99 and triangles from Ledwell et al. (1998); Watson and Ledwell (2000)]. In Fig. 10d, the triangle to the left corresponds to the first six months of the experiment while the one to the right corresponds to the next two years of measurements. The error bars of the NATRE data are also shown. The agreement between the model results and the data is satisfactory. In Fig. 11, we show the density ratio  $R_\rho$  versus  $z$  using the same NATRE data.

**14. Global ocean results**

Using the new model for the  $K_s$ , we obtain the results presented in Figs. 12–18. In Figs. 12–15, the Levitus et al. (1994) data are represented by the full line. We ran the code with both the  $K$  parameter parameterization (KPP) model ( $K_h = K_s$  and adjustable background diffusivities; Large et al. 1997) and our model. The diamonds correspond to the KPP model and the asterisks correspond to the present model. In Fig. 12 we plot the global average temperature. The new model yields a closer fit to Levitus data than previous models especially in the first 1 km. As for the salinity (Fig. 13), the new model improves the correspondence with Levitus data in the upper kilometer. In the Arctic Ocean (Fig. 14), the temperature profile is improved versus the KPP model; as for the salinity (Fig. 15), the new model brings about a considerable improvement over the KPP model

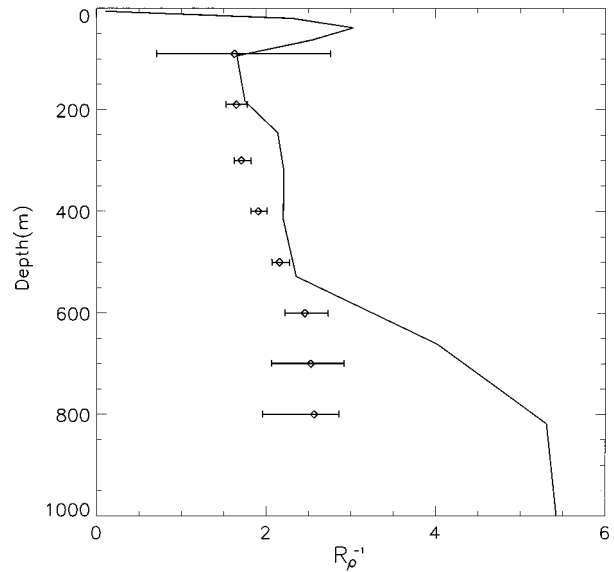


FIG. 11. Profile of the density ratio  $R_\rho$ , NATRE data (diamonds with error bars) and model results (full line).

in the ML where the KPP model indicated a freshening of the water masses. In Figs. 16, we present the North Atlantic overturning streamfunction (in Sv) with double diffusion (a) and without it (b). At  $24^\circ\text{N}$ , the presence of double diffusion yields a better fit to the measured values  $16 \pm 5$  Sv and  $17 \pm 4$  Sv (Roemmich and Wunsch 1985; Macdonald and Wunsch 1996). In Fig. 17, we show the polar heat transport in the North Atlantic (a), Indo–Pacific Ocean (b) and global ocean (c). The data, the symbols, and the error bars are from Macdonald and Wunsch (1996). As one can notice, while the agreement is generally acceptable, the presence of double diffusion has lowered the polar heat transport, a fact noticed by previous authors. To be more realistic, one must change the salinity boundary conditions from “restoring,” as used in part in the NCAR–CSM ocean model, to “natural” (Huang 1993) so as to ensure that there is no salt flux across the air–sea interface, as the physics of the problem requires. Jiang et al. (1999) used these boundary conditions, together with an updated set of  $E - P$  values, and showed that the heat transport increases by 23% while at  $24^\circ\text{N}$  the thermohaline circulation increases from 12 Sv to 27 Sv. These values correspond to the case of a horizontal diffusivity; if the latter is substituted with the Gent–McWilliams model, the 27 Sv value decreases to 21 Sv, which will get closer to the measured values once the effect of double diffusion is included. Finally, in Fig. 18, we present the model results for the freshwater budgets, which were computed as in Danabasoglu and McWilliams (1994). Generally, the new model gives similar results to KPP, but the magnitude of the transport in the North Atlantic has been noticeably reduced.



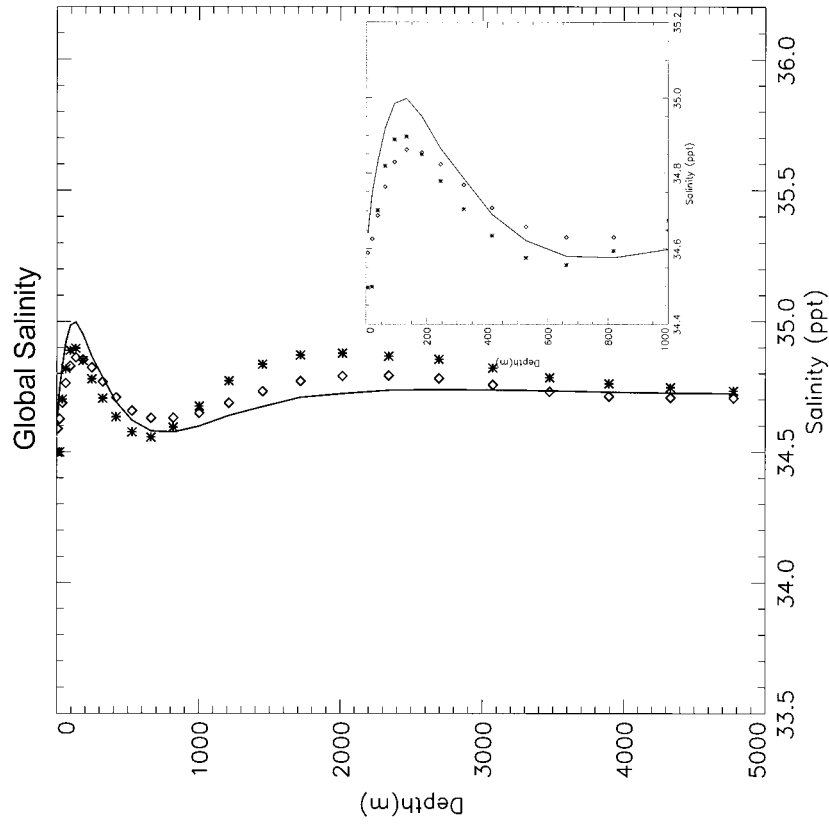


FIG. 13. As in Fig. 12 but for the global salinity profile.

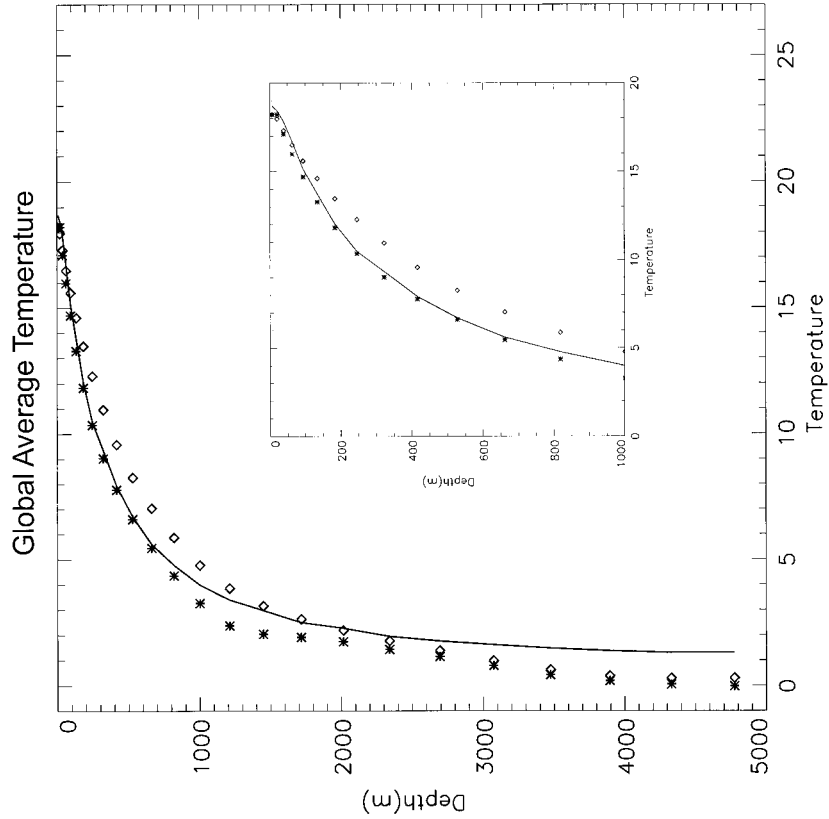


FIG. 12. The global ocean temperature using the NCAR OGCM. The Levitus et al. (1994) data are represented by a solid line. We have also run the code with the KPP model ( $K_p = K_h$ , Large et al. 1994) the results of which are represented by diamonds while the present model results are indicated by asterisks.

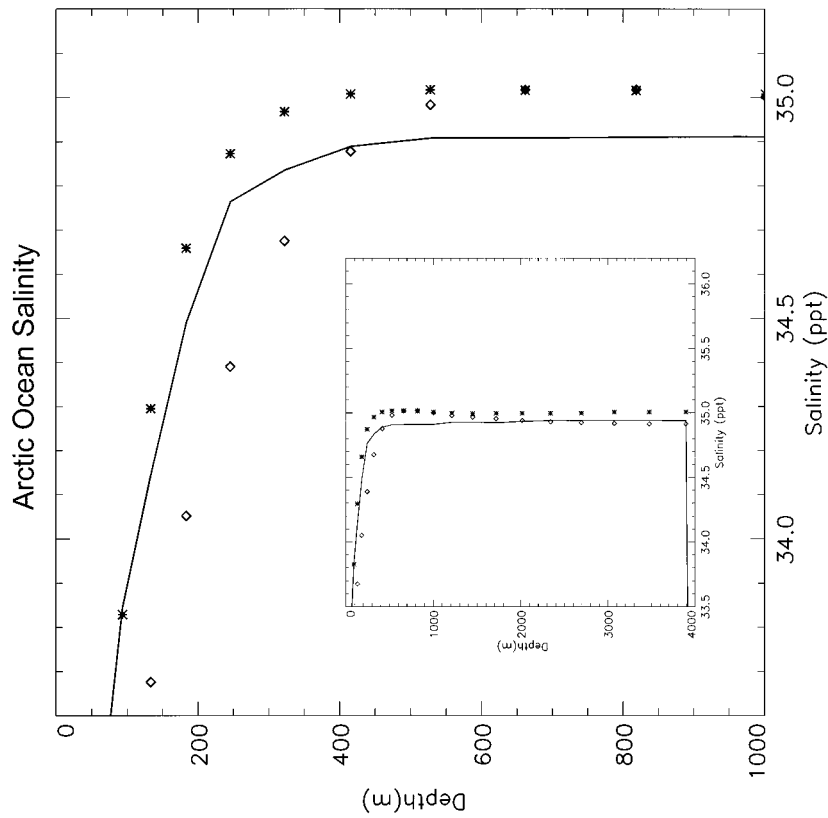


FIG. 15. As in Fig. 12 but for the Arctic Ocean salinity profile.

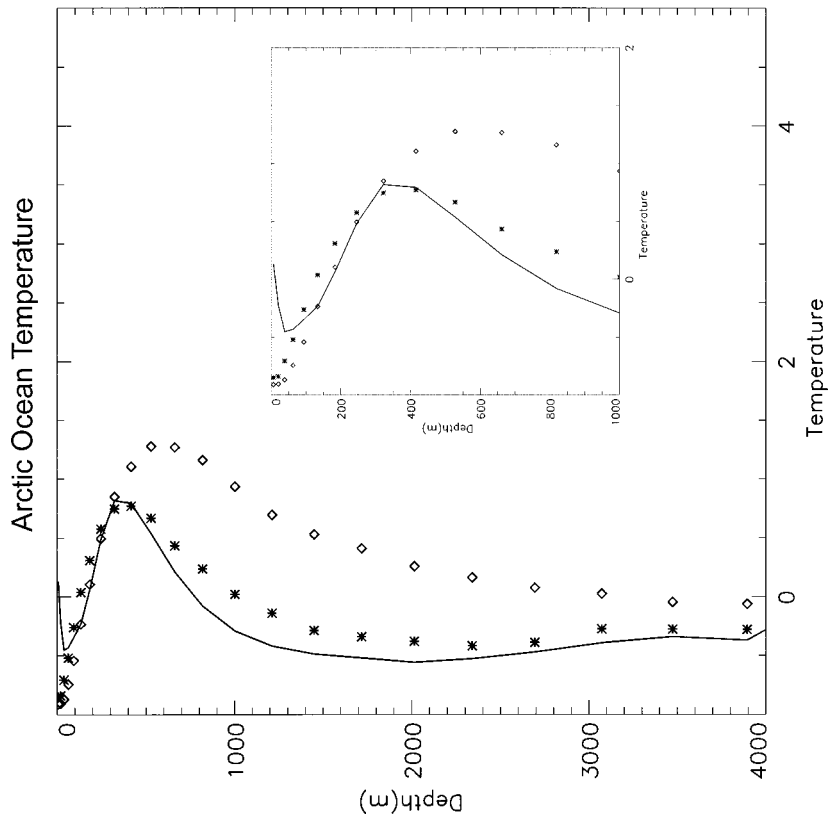


FIG. 14. As in Fig. 12 but for the Arctic Ocean temperature profile.

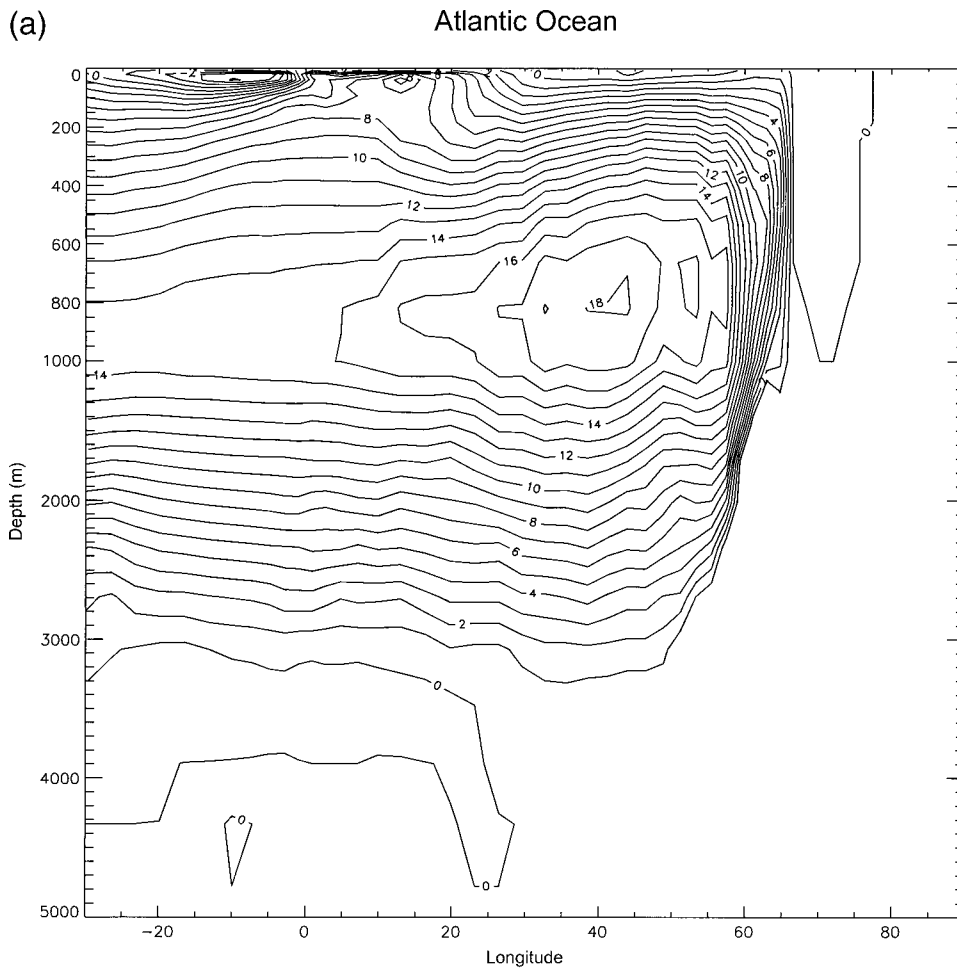


FIG. 16. The North Atlantic overturning streamfunction (in Sv) with double diffusion (a) and with the present model (b) but with  $K_s = K_h$

## 15. Discussion

Given the relevance of double-diffusion processes in the ocean, several authors have studied the phenomenon and its implications on ocean dynamics (Gargett and Holloway 1992; Zhang et al. 1998; Merryfield et al. 1999; Zhang and Schmitt 2000). While laboratory data on salt fingers (SF) are quite extensive, their utilization in an OGCM is not straightforward since oceanic SF occur in a complex environment where, for example, there are wave breaking processes. To account for both processes is a difficult task and different authors have used different approaches. The most recent model, Eqs. (25), is based on the following assumptions:

- 1) SF (salt fingers) and WR (wave regime, called turbulence) exist simultaneously,
- 2) SF and WR dominate in different regions separated by a critical  $R_\rho(\text{cr})$  below which WR dominate and above which SF dominate,
- 3) the expression for the SF diffusivities is taken from

phenomenological models (e.g., Schmitt 1981; Fedorov 1988; Kelly 1984, 1990),

- 4) the value of  $R_\rho(\text{cr})$  is empirically determined to be 0.64,
- 5) the term in (26a) contributed by wave braking has been taken alternatively as a constant or a function of the type  $a/N$ , Eq. (26b).

The present model is not based on the above assumptions and double diffusion and stirring by waves are treated within the same formalism, which also yields the value of  $R_\rho(\text{cr})$ . Interestingly enough, the results of the present model shown in Fig. 6 are very close to those of Fig. 2 of Walsh and Ruddick (2000). This is however more than a theoretical validation of model (25) since the latter is only valid for salt fingers whereas the present model encompasses all double diffusion processes. In addition, the combination SF + WR is not the only one in the ocean since, as discussed earlier, there is a variety of stirring sources in addition to wave breaking.

At a more basic level, there is a methodological dif-

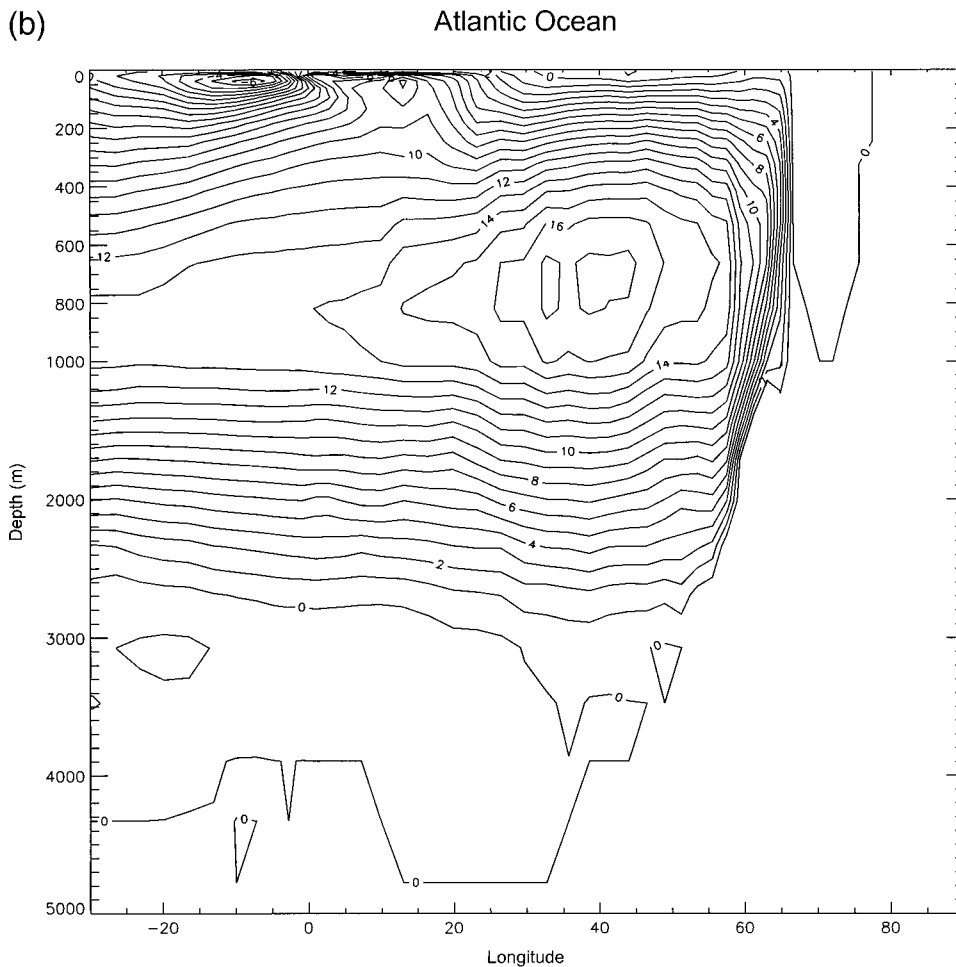


FIG. 16. (Continued)

ference. We have adopted an Osborn–Cox-like approach based on the dynamic equations, which we enlarged to include all the dynamic equations relevant to the presence of velocity, temperature, and salinity fields. The only methodology capable of doing so is the Reynolds stress model.

We have derived the expressions for the diffusivities of momentum, heat, and salt as a function of the Richardson number  $Ri^T$ , density ratio  $R_\rho$ , Brunt–Väisälä frequency  $N$ , and rate of dissipation of turbulent kinetic energy  $\epsilon$ . The model encompasses salt fingers, diffusive convection, and doubly stable and doubly unstable cases as well as shear. The latter, though of different origin at different depths, is always present in the ocean. Within the mixed layer, it is due to external winds while in the ocean interior, it may be due to a variety of sources. The model is valid in both the ML and below it in the sense that the functional dependence of the diffusivities on the variables  $Ri^T$ ,  $R_\rho$ ,  $N$ , and  $\epsilon$  is the same throughout the vertical extent of the ocean. What is different between the ML and thermocline (and below it) is the modeling of  $Ri^T$  and  $\epsilon$ .

**16. Future improvements of the model**

The major difficulty in constructing this model was the evaluation of the dissipation timescales. Since the presence of salt fingers is an indication that molecular effects are important, one is called upon to construct a model that is atypical since most turbulence models assume negligible molecular effects. The weak and strong turbulence models presented earlier represent two extremes and neither one is representative of ocean mixing. What is required is a model that encompasses both limits but such a model is still not available. In our approach, the molecular/turbulence interface is represented by a single variable, the correlation timescale  $\tau_{s\theta}$  whose value from the turbulence model was slightly too large. A 10% decrease was sufficient to reproduce the correct value of  $R_\rho(cr)$ . The theoretical challenge is how to compute  $\tau_{s\theta}$  from a two-point closure model.

The present model is local since Eqs. (5)–(11) do not contain the third-order moments (TOM), for example,  $u_i'' T''^2$ , that would appear in the left-hand side of Eq.

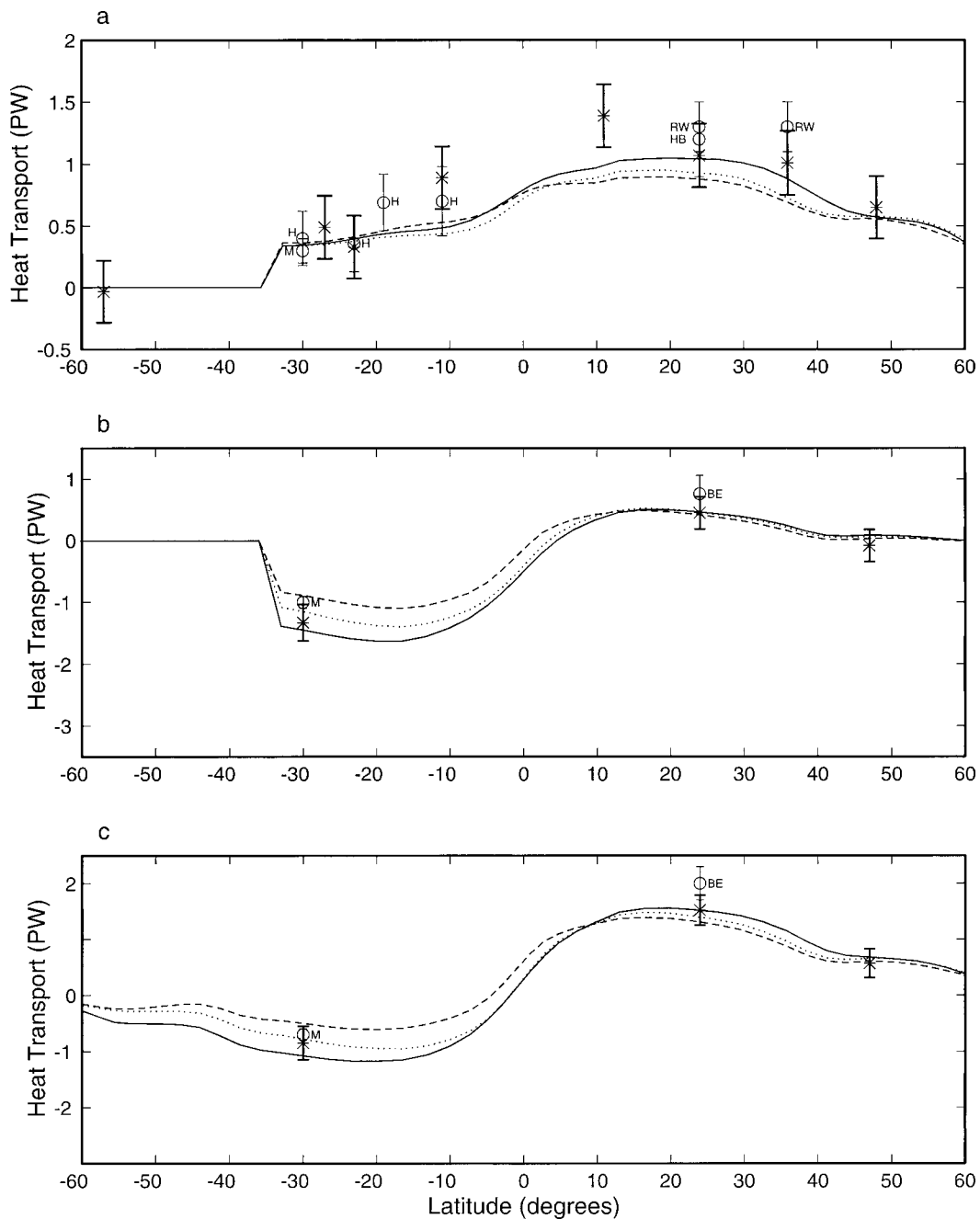


FIG. 17. Polar heat transport vs latitude for (a) the North Atlantic Ocean, (b) the Indo-Pacific Ocean, and (c) the global ocean. The data from different authors and the error bars are from Macdonald and Wunsch (1996). Solid line (KPP model,  $K_s = K_b$ ), dotted line (present model with  $K_s = K_b$ ), dashed line (present model with  $K_s \neq K_b$ ). Double diffusion ( $K_b \neq K_s$ ) lowers the value of the heat flux, a conclusion in agreement with previous authors.

(7). The presence of nonlocal terms would change the heat flux expression in (2d) to

$$\overline{w''T''} = -K_h \left( \frac{\partial T}{\partial z} + \Gamma \right), \quad (27a)$$

where  $\Gamma$ , known as the countergradient term, is a function of the TOMs. Since a new, algebraic expression for

the TOMs has recently been derived (Canuto et al. 1994; Canuto et al. 2001a), the present model can be made nonlocal.

Finally, the treatment of wave-turbulence interaction can also be improved. In fact, one may further split any turbulent variable  $\phi''$  as

$$\phi'' = \phi''_i + \phi''_w, \quad (27b)$$

where the subscripts  $t$  and  $w$  stand for turbulence and waves. This has already been done in the atmospheric context (Finnigan and Einaudi 1981) and it could also be applied here with an unavoidable increase in the number of equations to solve. However, it may be an effort worth pursuing because of the new physical insight one may gain from it.

*Acknowledgments.* The authors would like to thank three referees who greatly helped improve the manuscript. Dr. G. Holloway suggested the test discussed in section 12.

APPENDIX A

Functions in Eqs. (13)–(14)

Using the abbreviated notation:

$$\begin{aligned}
 p_{1m} &= 1 - p_1, & p_{2m} &= 1 - p_2, & p_3 &= \frac{5}{2} \pi_1, \\
 p_4 &= \frac{1}{5} \pi_1 \pi_3^{-2}, & p_5 &= \pi_1 \pi_2 \pi_3^{-2}, \\
 p_6 &= \frac{1}{5} \pi_3^{-1} \pi_2^{-1} \pi_4, & p_7 &= 5 \pi_2, & p_8 &= \frac{5}{2} \pi_4, \\
 p_9 &= \pi_5 \pi_4 (\pi_3 \pi_2)^{-1}, & p_{10} &= \pi_2 \pi_4 \pi_3^{-2}, \\
 p_{11} &= \pi_1 \pi_3^{-1}
 \end{aligned}
 \tag{A1}$$

the functions  $a_k$ ,  $b_k$ , and  $d_k$  entering Eqs. (13)–(14) are given by

$$\begin{aligned}
 a_1 &= p_{11}[12p_9 + 8p_6 - 30p_6p_8 - 5p_6(p_{1m} + 3p_{2m})] \\
 a_2 &= [8 - 5(p_{1m} + 3p_{2m})](p_4p_9 + p_6p_{11} - 2p_5p_6) \\
 &\quad + 12p_{11}p_9 \\
 &\quad - 30(p_3p_4p_9 + p_6p_8p_{11} - p_5p_6p_8 - p_3p_5p_6) \\
 a_3 &= p_{10}[8p_4 + 12p_{11} - 30p_3p_4 - 5p_4(p_{1m} + 3p_{2m})] \\
 a_4 &= -p_6(8 - 30p_8 - 5p_{1m} - 15p_{2m}) - 12(p_9 + p_{11}) \\
 a_5 &= -p_4(8 - 30p_3 - 5p_{1m} - 15p_{2m}) - 12(p_{10} + p_{11})
 \end{aligned}
 \tag{A2}$$

$$\begin{aligned}
 b_1 &= \pi_1 \pi_3^{-2} (\pi_2 - \pi_3), & b_2 &= -\pi_1 \pi_3^{-1}, \\
 b_3 &= 15p_{2m}^2 + 2p_{1m} - 5p_{1m}^2 - 6p_{2m}, & b_4 &= -6\pi_1 \pi_3^{-2}, \\
 b_5 &= -6\pi_4 \pi_2^{-1} \pi_3^{-1} & b_6 &= -\pi_2 \pi_4 \pi_3^{-2} \\
 b_7 &= \pi_4 \pi_2^{-1} \pi_3^{-1} (\pi_2 - \pi_5)
 \end{aligned}
 \tag{A3}$$

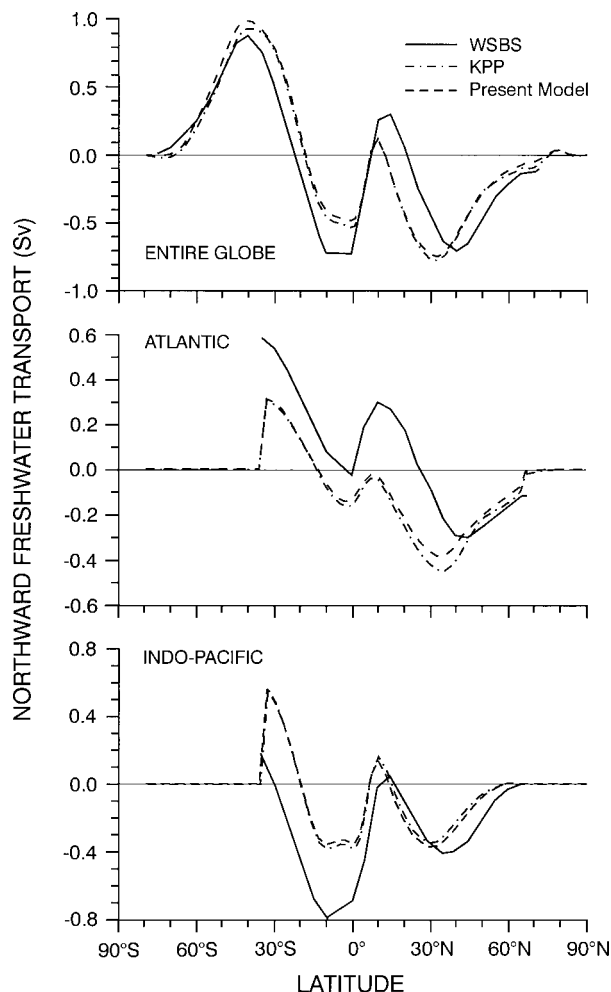


FIG. 18. Freshwater budget. The WSBS curve corresponds to the measurements of Wijffels et al. (1992) as presented in Large et al. (1997).

$$\begin{aligned}
 d_1 &= p_{11}[p_{2m}^2(p_6 + 6p_9) + 2(p_{1m} - 3p_{2m})p_6p_8 \\
 &\quad - p_{1m}^2(p_6 + 2p_9)] \\
 d_2 &= (p_{1m}^2 - p_{2m}^2)(2p_5p_6 - p_6p_{11} - p_4p_9) \\
 &\quad + 2(p_{1m}^2 - 3p_{2m}^2)(p_5p_6p_7 - p_{11}p_9 - p_{10}p_{11}) \\
 &\quad + 2(p_{1m} - 3p_{2m}) \\
 &\quad \times (p_3p_4p_9 + p_6p_8p_{11} - p_5p_6p_8 - p_3p_5p_6) \\
 d_3 &= p_{10}[p_{2m}^2(p_4 + 6p_{11}) + 2(p_{1m} - 3p_{2m})p_3p_4 \\
 &\quad - p_{1m}^2(p_4 + 2p_{11})] \\
 d_4 &= -4p_6p_{11}(2p_6 + 3p_9) \\
 d_5 &= 4p_4p_7p_6^2(4 + 3p_7) - 4p_4p_9(3p_{11} + 2p_6) \\
 &\quad - 4p_6p_{11}(3p_9 + 3p_{10} + 2p_4 + 2p_6)
 \end{aligned}$$

$$\begin{aligned}
d_6 &= 4p_4^2 p_6 p_7 (4 + 3p_7) - 4p_4 p_9 (2p_4 + 3p_{11}) \\
&\quad - 8p_4 p_6 (p_{10} + p_{11}) - 12p_{10} p_{11} (p_4 + p_6) \\
d_7 &= -4p_4 p_{10} (2p_4 + 3p_{11}) \\
d_8 &= p_{1m}^2 (2p_9 + 2p_{11} + p_6) - p_{2m}^2 (6p_9 + 6p_{11} + p_6) \\
&\quad - 2p_6 p_8 (p_{1m} - 3p_{2m}) \\
d_9 &= p_{1m}^2 (2p_{11} + 2p_{10} + p_4) - p_{2m}^2 (6p_{11} + 6p_{10} + p_4) \\
&\quad - 2p_3 p_4 (p_{1m} - 3p_{2m}) \\
d_{10} &= 8p_6^2 + 4p_6 (3p_9 + 7p_{11}) + 24p_9 p_{11} \\
d_{11} &= -8p_5 p_6 (4 + 3p_7) + 4p_4 (4p_6 + 7p_9 + 3p_{11}) \\
&\quad + 4p_6 (3p_{10} + 7p_{11}) + 24p_{11} (p_9 + p_{10}) \\
d_{12} &= 4p_{10} (7p_4 + 6p_{11}) + 4p_4 (2p_4 + 3p_{11}) \\
d_{13} &= 6p_{2m}^2 - 2p_{1m}^2 \quad d_{14} = -24p_9 - 24p_{11} - 28p_6 \\
d_{15} &= -24p_{11} - 24p_{10} - 28p_4. \tag{A4}
\end{aligned}$$

## APPENDIX B

## Values of the Constants in Eqs. (13)–(15)

In the present model, the  $\pi_s$  are given by Eqs. (22d):

$$\pi_1 = \pi_4 = 0.08372, \quad \pi_2 = 1/3, \quad \pi_3 = \pi_5 = 0.72, \tag{B1}$$

and

$$p_1 = 0.832, \quad p_2 = 0.545. \tag{B2}$$

Thus, the  $p_k$ ,  $a_k$ ,  $b_k$ , and  $d_k$  of appendix A take the numerical values:

$$\begin{aligned}
p_3 &= 0.2093, & p_4 &= 0.0323, & p_5 &= 0.0538, \\
p_6 &= 0.0698, & p_7 &= 1.6666, & p_8 &= 0.2093, \\
p_9 &= 0.2511, & p_{10} &= 0.0538, \\
p_{11} &= 0.1163, \tag{B3}
\end{aligned}$$

$$\begin{aligned}
a_1 &= 0.3022, & a_2 &= 0.2986, & a_3 &= 0.06478, \\
a_4 &= -3.99459, & a_5 &= -1.8493, \tag{B4}
\end{aligned}$$

$$\begin{aligned}
b_1 &= -0.0625, & b_2 &= -0.1163, & b_3 &= 0.5702, \\
b_4 &= -0.9689, & b_5 &= -2.0930, \\
b_6 &= -0.0538, & b_7 &= -0.13488, \tag{B5}
\end{aligned}$$

$$\begin{aligned}
d_1 &= 0.03201, & d_2 &= 0.0318, \\
d_3 &= 0.00686, & d_4 &= -0.0289, \\
d_5 &= -0.04272, & d_6 &= -0.01978, \\
d_7 &= -0.002875, & d_8 &= -0.41319, \\
d_9 &= -0.1912, & d_{10} &= 1.1773, \\
d_{11} &= 1.1612, & d_{12} &= 0.2523, \\
d_{13} &= 1.1857, & d_{14} &= -10.7721, \\
d_{15} &= -4.9871. \tag{B6}
\end{aligned}$$

## APPENDIX C

The Function  $f(R_\rho)$ , Eq. (23a)

The function  $f(R_\rho)$  of Eq. (23a) is given by

$$f(R_\rho) = f_1 f_2^{-1} \tag{C1}$$

$$\begin{aligned}
f_1 &= 2a_m(1 - R_\rho) - 5(\pi_4 \alpha_2 - \pi_1 \alpha_4 R_\rho) \\
&\quad - 6\delta_0(1 - R_\rho) \tag{C2}
\end{aligned}$$

$$f_2 = 6\delta_1(1 - R_\rho) + 5(\pi_4 \alpha_1 - \pi_1 \alpha_3 R_\rho), \tag{C3}$$

where

$$\begin{aligned}
a_m &= a_1 N_0^2 + a_2 N_0 C_0 + a_3 C_0^2 \\
\alpha_1 &= b_1 b_4 C_0^2 + (b_1 b_5 + b_2 b_4) N_0 C_0 + b_2 b_5 N_0^2 \\
\alpha_2 &= b_1 b_3 C_0 + b_2 b_3 N_0 \\
\alpha_3 &= b_4 b_6 C_0^2 + (b_5 b_6 + b_4 b_7) N_0 C_0 + b_5 b_7 N_0^2 \\
\alpha_4 &= b_3 b_6 C_0 + b_3 b_7 N_0 \\
\delta_0 &= d_1 N_0^2 + d_2 N_0 C_0 + d_3 C_0^2 \\
\delta_1 &= d_4 N_0^3 + d_5 C_0 N_0^2 + d_6 N_0 C_0^2 + d_7 C_0^3 \\
N_0 &= -\frac{25}{4} \pi_2 \pi_3 (1 - R_\rho)^{-1} \\
C_0 &= \frac{25}{4} \pi_3^2 R_\rho (1 - R_\rho)^{-1}. \tag{C4}
\end{aligned}$$

## REFERENCES

- Adcroft, A., J. R. Scott, and J. Marotzke, 2001: Impact of geothermal heating on the global ocean circulation. *Geophys. Res. Lett.*, **28**, 1735–1738.
- Armi, L., and R. C. Millard Jr., 1976: The bottom boundary layer of the deep ocean. *J. Geophys. Res.*, **81**, 4983–4990.
- Bell, T. H., Jr., 1975: Topographically generated internal waves in the open ocean. *J. Geophys. Res.*, **80**, 320–327.
- Blackadar, A. K., 1962: The vertical distribution of wind and turbulent exchange in neutral atmosphere. *J. Geophys. Res.*, **67**, 3095–3102.
- Burchard, H., and K. Bolding, 2001: Comparative analysis of four

- second moment turbulence closure models for the oceanic mixed layer. *J. Phys. Oceanogr.*, **31**, 1943–1968.
- , and E. Deleersnijder, 2001: Stability of algebraic non-equilibrium second-moment turbulence closure models. *Ocean Modelling*, **3**, 33–50.
- , O. Peterson, and T. P. Rippeth, 1998: Comparing the performance of the Mellor–Yamada and the K- $\epsilon$  two equation turbulence models. *J. Geophys. Res.*, **103**, 10 543–10 554.
- Canuto, V. M., and M. S. Dubovikov, 1996a: A dynamical model for turbulence: I. General formalism. *Phys. Fluids*, **8**, 571–586.
- , and —, 1996b: A dynamical model for turbulence: II. Shear-driven flows. *Phys. Fluids*, **8**, 587–598.
- , and —, 1997: A dynamical model for turbulence: IV. Buoyancy driven flows. *Phys. Fluids*, **9**, 2118–2131.
- , F. Minotti, C. Ronchi, R. M. Ypma, and O. Zeman, 1994: Second-order closure PBL model with new third-order moments. Comparison with LES data. *J. Atmos. Sci.*, **51**, 1605–1618.
- , Y. Cheng, and A. Howard, 2001a: New third-order moments for the CBL. *J. Atmos. Sci.*, **58**, 1169–1172.
- , A. Howard, Y. Cheng, and M. S. Dubovikov, 2001b: Ocean Turbulence. Part I: One-point closure model. Momentum and heat vertical diffusivities. *J. Phys. Oceanogr.*, **31**, 1413–1426.
- Cheng, Y., and V. M. Canuto, 1994: Stably stratified shear turbulence: A new model for the energy dissipation length scale. *J. Atmos. Sci.*, **51**, 2384–2396.
- Danabasoglu, G., and J. C. McWilliams, 1995: Sensitivity of the global ocean circulation to parameterizations of mesoscale tracer transport. *J. Climate*, **8**, 2967–2987.
- D’Asaro, E. A., and R.-C. Lien, 2000a: Lagrangian measurements of waves and turbulence in stratified flows. *J. Phys. Oceanogr.*, **30**, 641–655.
- , and —, 2000b: The wave–turbulence transition for stratified flows. *J. Phys. Oceanogr.*, **30**, 1669–1678.
- Davis, R. E., 1994a: Diapycnal mixing in the ocean: Equations for the large scale budgets. *J. Phys. Oceanogr.*, **24**, 777–800.
- , 1994b: Diapycnal mixing in the ocean: The Osborn–Cox Model. *J. Phys. Oceanogr.*, **24**, 2560–2576.
- Deardorff, J. W., 1980: Stratocumulus-capped mixed layer derived from a 3D model. *Bound.-Layer Meteor.*, **18**, 495–502.
- Desaubies, Y., and W. K. Smith, 1982: Statistics of Richardson number and instabilities in oceanic internal waves. *J. Phys. Oceanogr.*, **12**, 1245–1259.
- Egbert, G. D., and R. D. Ray, 2000: Significant dissipation of tidal energy in the deep ocean inferred from satellite data. *Nature*, **405**, 775–778.
- Fedorov, K. N., 1988: Layer thickness and effective diffusivities in “diffusive” thermohaline convection in the ocean. *Small Scale Turbulence and Mixing in the Ocean*, J. Nihoul and B. Jamart, Eds., Vol. 46, Elsevier, 471–480.
- Finnigan, J. J., and F. Einaudi, 1981: The interaction between an internal gravity wave and the planetary boundary layer. Part II: Effect of the wave on the turbulence structure. *Quart. J. Roy. Meteor. Soc.*, **107**, 807–832.
- Gargett, A. E., and G. Holloway, 1992: Sensitivity of the GFDL ocean model to different diffusivities for heat and salt. *J. Phys. Oceanogr.*, **22**, 1158–1177.
- , and B. Ferron, 1996: The effect of differential vertical diffusion of T and S in a box model of thermohaline circulation. *J. Mar. Res.*, **54**, 827–866.
- Garret, C. J. R., and W. H. Munk, 1975: Space–time scales of internal waves: A progress report. *J. Geophys. Res.*, **80**, 291–297.
- Gatski, T. B., S. Sarkar, and C. G. Speziale, 1993: *Studies in Turbulence*. Springer Verlag, 602 pp.
- Gregg, M. C., 1987: Diapycnal mixing: A review. *J. Geophys. Res.*, **92**, 5249–5286.
- , 1989: Scaling turbulent dissipation in the thermocline. *J. Geophys. Res.*, **94**, 9689–9698.
- , D. P. Winkel, T. S. Sanford, and H. Peters, 1996: Turbulence produced by internal waves in the oceanic thermocline at mid and low latitudes. *Dyn. Atmos. Oceans*, **24**, 1–14.
- Heney, F. S., J. Wright, and S. M. Flatte, 1986: Energy and action flow through the internal wave field. An eikonal approximation. *J. Geophys. Res.*, **91**, 8487–8495.
- Huang, R. X., 1993: Real freshwater flux as the upper boundary condition for the salinity balance and the thermocline circulation forced by evaporation and precipitation. *J. Phys. Oceanogr.*, **23**, 2428–2446.
- Jayne, S. R., and L. C. St. Laurent, 2001: Parameterizing tidal dissipation over rough topography. *Geophys. Res. Lett.*, **28**, 811–814.
- Jiang, S., P. H. Stone, and P. Malanotte-Rizzoli, 1999: An assessment of the GFDL ocean model with coarse resolution: Annual-mean climatology. *J. Geophys. Res.*, **104**, 25 623–25 645.
- Kelley, D. E., 1984: Effective diffusivities within oceanic thermohaline staircases. *J. Geophys. Res.*, **89**, 10 484–10 488.
- , 1990: Fluxes through diffusive staircases: A new formulation. *J. Geophys. Res.*, **95**, 3365–3371.
- Kunze, E., 1987: Limits to growing, finite-length salt fingers: A Richardson number constraint. *J. Mar. Res.*, **45**, 533–556.
- , 1990: The evolution of salt fingers in inertial wave shear. *J. Mar. Res.*, **48**, 471–504.
- , and T. S. Sanford, 1996: Abyssal mixing: Where it is not. *J. Phys. Oceanogr.*, **26**, 2286–2296.
- , and J. M. Toole, 1997: Tidally driven vorticity, diurnal shear and turbulence atop Fieberling Seamount. *J. Phys. Oceanogr.*, **27**, 2663–2693.
- Large, W. G., J. C. McWilliams, and S. C. Doney, 1994: Oceanic vertical mixing: A review and a model with non-local boundary layer parameterization. *Rev. Geophys.*, **32**, 363–403.
- , G. Danabasoglu, S. C. Doney, and J. C. McWilliams, 1997: Sensitivity to surface forcing and boundary layer mixing in a global ocean model: Annual-mean climatology. *J. Phys. Oceanogr.*, **27**, 2418–2447.
- Ledwell, J. R., A. J. Watson, and C. S. Law, 1993: Evidence for slow mixing across the pycnocline from an open ocean tracer-release experiment. *Nature*, **364**, 701–703.
- , —, and —, 1998: Mixing of a tracer in the pycnocline. *J. Geophys. Res.*, **103**, 21 499–21 529.
- , E. T. Montgomery, K. L. Polzin, L. St. Laurent, R. W. Schmitt, and J. M. Toole, 2000: Evidence for enhanced mixing over rough topography in the abyssal ocean. *Nature*, **403**, 179–182.
- Levitus, S., and T. P. Boyer, 1994: *World Ocean Atlas 1994*. Vol. 4: *Temperature*, NOAA Atlas NESDIS 4, 129 pp.
- , R. Burgett, and T. P. Boyer, 1994: *World Ocean Atlas 1994*. Vol. 3: *Salinity*, NOAA Atlas NESDIS3, 99 pp.
- McDonald, A. M., and C. Wunsch, 1996: An estimate of global ocean circulation and heat fluxes. *Nature*, **382**, 436–439.
- McComas, C. H., and P. Muller, 1981: The dynamic balance of internal waves. *J. Phys. Oceanogr.*, **11**, 970–986.
- McDougall, T., and B. Ruddick, 1992: The use of ocean microstructure to quantify both turbulent mixing and salt-fingers. *Deep-Sea Res.*, **11/12**, 1931–1952.
- Mellor, G. L., and T. Yamada, 1982: Development of a turbulence closure model for geophysical fluid problems. *Rev. Geophys. Space Phys.*, **20**, 851–875.
- Merryfield, W. J., G. Holloway, and A. E. Gargett, 1998: Differential vertical transport of heat and salt by weak stratified turbulence. *Geophys. Res. Lett.*, **25**, 2773–2776.
- , —, and —, 1999: A global ocean model with double diffusive mixing. *J. Phys. Oceanogr.*, **29**, 1124–1142.
- Monin, A. S., and A. M. Yaglom, 1971: *Statistical Fluid Mechanics: Mechanics of Turbulence*. Vol. 1, The MIT Press, 769 pp.
- , and —, 1975: *Statistical Fluid Mechanics: Mechanics of Turbulence*. Vol. 2, The MIT Press, 874 pp.
- Moum, J. N., and T. R. Osborn, 1986: Mixing in the main thermocline. *J. Phys. Oceanogr.*, **16**, 125–129.
- Müller, P., and N. Xu, 1992: Scattering of oceanic internal gravity waves off random bottom topography. *J. Phys. Oceanogr.*, **22**, 474–488.
- Munk, W. H., 1966: Abyssal recipes. *Deep-Sea Res.*, **13**, 707–730.



- , 1981: Internal waves and small scale processes. *Scientific Surveys in Honor of H. Stommel*, B. A. Warren and C. Wunsch, Eds., The MIT Press, 264–291.
- , and C. Wunsch, 1998: Abyssal recipes II: Energetics of tidal and wind mixing. *Deep-Sea Res. I*, **45**, 1977–2110.
- Osborn, T. R., 1980: Estimates of the local rate of vertical diffusion from dissipation measurements. *J. Phys. Oceanogr.*, **10**, 83–89.
- , and C. S. Cox, 1972: Oceanic fine structure. *Geophys. Fluid Dyn.*, **3**, 321–345.
- Polzin, K., 1996: Statistics of the Richardson number: Mixing models and fine structure. *J. Phys. Oceanogr.*, **26**, 1409–1425.
- , J. M. Toole, and R. W. Schmitt, 1995: Finescale parameterization of turbulent dissipation. *J. Phys. Oceanogr.*, **25**, 306–328.
- , J. R. Ledwell, and R. W. Schmitt, 1997: Spatial variability of turbulent mixing in the abyssal ocean. *Science*, **276**, 93–96.
- Roemmich, D., and C. Wunsch, 1985: Two transatlantic sections: Meridional circulation and heat flux in the subtropical North Atlantic Ocean. *Deep-Sea Res.*, **32**, 619–664.
- Schmitt, R. W., 1981: Form of the T–S relationship in central waters: Evidence for double diffusive mixing. *J. Phys. Oceanogr.*, **11**, 1015–1026.
- , 1994: Double diffusion in oceanography. *Ann. Rev. Fluid Dyn.*, **26**, 255–285.
- , and D. L. Evans, 1978: An estimate of the vertical mixing due to salt fingers based on observations in the North Atlantic central waters. *J. Geophys. Res.*, **83**, 2913–2919.
- St. Laurent, L., and R. W. Schmitt, 1999: The contribution of salt fingers to vertical mixing in the NATRE experiment. *J. Phys. Oceanogr.*, **29**, 1404–1424.
- Stern, M. E., 1975: *Ocean Circulation Physics*. Academic Press, 246 pp.
- Sun, H., and E. Kunze, 1999a: Internal wave–wave interactions. Part I: The role of internal wave vertical divergence. *J. Phys. Oceanogr.*, **29**, 2886–2904.
- , and —, 1999b: Internal wave–wave interactions. Part II: Spectral energy transfer and turbulence production. *J. Phys. Oceanogr.*, **29**, 2905–2919.
- Toole, J. M., 1998: Turbulent mixing in the ocean. *Ocean Modeling and Parameterization*, E. P. Chassignet and J. Verron, Eds., NATO Science Series, Vol. 516, Kluwer Academic, 171–190.
- Walsh, D., and B. Ruddick, 2000: Double-diffusion interleaving in the presence of turbulence. The effect of a nonconstant flux ratio. *J. Phys. Oceanogr.*, **30**, 2231–2245.
- Watson, A. J., and J. R. Ledwell, 2000: Oceanographic tracer release experiments using SF. *J. Geophys. Res.*, **105**, 14 325–14 337.
- Wijffels, E. E., R. W. Schmitt, H. L. Bryden, and A. Stigebrandt, 1992: Transport of freshwater by the oceans. *J. Phys. Oceanogr.*, **22**, 155–162.
- Wunsch, C., 2000: Moon, tides and climate. *Nature*, **405**, 743–744.
- Zeman, O., and J. L. Lumley, 1982: Modeling salt-fingers structures. *J. Mar. Res.*, **40**, 315–330.
- , and —, 1983: Progress in modeling multilayer salt-fingers structures. *Math. Model.*, **4**, 73–85.
- Zhang, J., and R. Schmitt, 2000: The impact of salt fingering on the thermohaline circulation under mixed boundary conditions. *J. Phys. Oceanogr.*, **30**, 1223–1231.
- , —, and R. X. Huang, 1998: Sensitivity of the GFDL ocean model to parameterization of double-diffusion processes. *J. Phys. Oceanogr.*, **28**, 589–605.
- , —, and —, 1999: The relative influence of diapycnal mixing and hydrological forcing on the stability of the thermocline circulation. *J. Phys. Oceanogr.*, **29**, 1096–1108.